Manuel Rocha Medal Recipient

Rock Fracture and Collapse Under Low Confinement Conditions

By

M. S. Diederichs

Department of Geological Sciences and Geological Engineering,
Queen's University, Kingston, Ontario, Canada

This paper summarizes some of the work presented by Dr. M. S. Diederichs during the ISRM Rocha Medal ceremony at the ISRM International Symposium, EUROCK 2002, in Madeira during November 2002. Dr. Diederichs was born and educated in Canada and received his PhD from the University of Waterloo in 2000. He is currently an Assistant Professor in the Dept. Geological Sciences and Geological Engineering at Queen's University and is a member of the Geo-Engineering Research Centre at Queen's and RMC (www.geoeng.ca).

Summary

The primary objective of this work was an examination of the complimentary roles of tensile damage and confinement reduction (or stress relaxation) on excavation response of "hard" rock-masses. Tensile damage and relaxation are examined with respect to structurally controlled or gravity driven failure modes as well as to strength controlled or stress driven rockmass damage and yield. In conventional analysis of both structurally controlled and stress driven failure, the effects of tensile damage and tensile resistance as well as the elevated sensitivity to low confinement are typically neglected, leading to erroneous predictions of groundfall potential or rock yield. The important role of these two elements in underground excavation stability in hard rock environments is examined in detail through a review of testing data, case study examination and a number of analytical and numerical analogues including discrete element simulation, statistical theory and fracture mechanics. This rigorous theoretical treatment updates, validates and constrains the current use of semi-empirical design guidelines based on these mechanisms.

Keywords: Rock fracture, strength, discrete elements, underground stability.

1. Introduction

Rockmass instability in underground excavations, from an engineering point of view, can be classified as structurally controlled gravity driven fallout or as strength controlled stress driven rockmass yield. The dominant behaviour is a function of the relative in situ stress and degree of jointing and fracturing in the rockmass. This work deals with both behavioural extremes in massive to moderately jointed rockmasses with ubiquitous structure. Instability caused by the presence of continuous faults and discrete shear features and rock failure in squeezing conditions are not considered here.

While structural analyses normally consider full persistence of bounding discontinuities, non-persistent jointing is more common at depth in hard rocks, away from major fault or folding zones, where the mechanics of tectonic joint development are essentially strain controlled, leading to stable fracture conditions such as those described theoretically by Ingraffea (1987). As will be demonstrated, intact rock bridges, in hard rock formations, need only occupy a very small percentage of the joint-coplanar area in order to provide internal or self-supporting load carrying capacity equivalent to conventional underground support systems. Consideration of this internal support mechanism, at least for short-term or ''first-pass'' applications, could lead to reduced primary support requirements and more efficient tunnel development. In Fig. 1a, the joint-normal tensile strength allows load transfer normal to a wedge-bounding surface or to laminations. This affords direct gravity support in the first case and effectively thickens the active beam in the second, laminated, case – increasing stability in both situations.
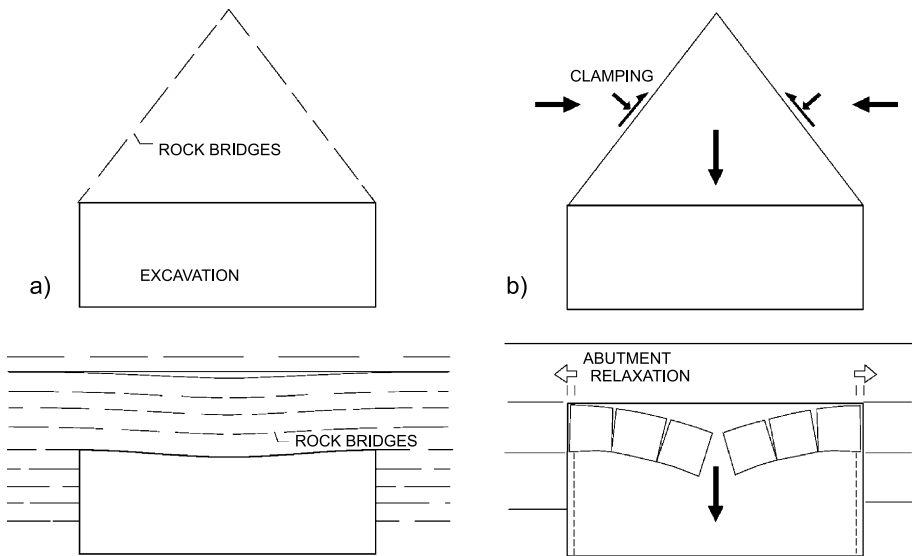
Fig. 1. Issues for structural instability examined in this work: **a**) Residual tensile strength due to rock bridges; **b**) Excavation-parallel confinement (top) and abutment relaxation (bottom)
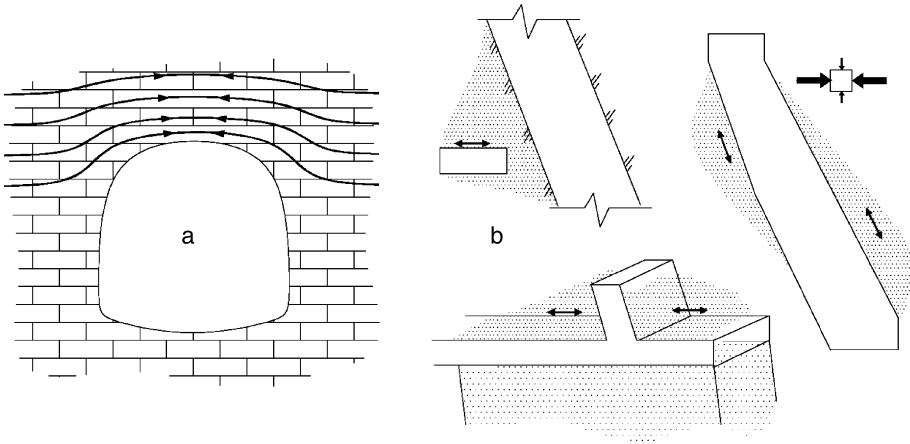
Fig. 2. a) Increased confinement around well-designed civil excavation; **b)** relaxation or confinement loss (shaded areas) due to complex mining geometries

Delayed failure in mining environments is often the result of induced abutment relaxation. This is considered in the cases of wedge instability and fallout of blocky rockmasses as in Fig. 1b. Changes in rock quality, excavation geometry, mining induced stress changes or surface deflection can lead to relaxation induced collapse of otherwise stable rockmasses. It is necessary to recognize the potential for this mechanism in order to improve mine sequencing and support design to minimize these types of failures. This is an issue of particular importance to mining. In civil engineering applications at low or moderate depth (tunnels, caverns, etc), roof geometries are typically arched to attract compression or clamping in the roof, thereby increasing stability (Fig. 2a). In contrast, complex mining geometries, driven by operational constraints and orebody geometries actually reduce confinement and induce structural instability (Fig. 2b).

In the case of stress driven failure, commonly applied shear-based geomechanical constitutive models have proven to be limited in their ability to accurately represent in situ failure of massive or moderately jointed rockmasses at depth around excavations. Past research has suggested that the origins of compressive damage and yield in hard rocks such as granite are tensile in nature (Brown and Trollope, 1967; Hoek, 1968; Tapponier and Brace, 1976; Stacey, 1981; etc.), induced by extension strain normal to the direction of maximum compression, σ_1. Microcracks, once initiated, tend to propagate parallel to σ_1 or, more correctly, normal to σ_3. An understanding of this damage process is essential in order to explain the observed in situ strength of hard rockmasses. The role of internal tensile fracture and extension cracking (Fig. 3a) on rock damage and yield under high, compressive stress is explored in this work. Of particular interest is the process of spalling around deep excavations in hard rock (Fig. 3b). The dominant role, under low confining stresses resulting from excavation, of this form of damage initiation and propagation (Fig. 3c) in hard rock yield processes is investigated and verified. The initiation of crack damage is relatively insensitive to confinement ($I_1 = \sigma_1 + \sigma_2 + \sigma_3$ or simply $\sigma_1 + \sigma_3$ in two dimensions). A ratio
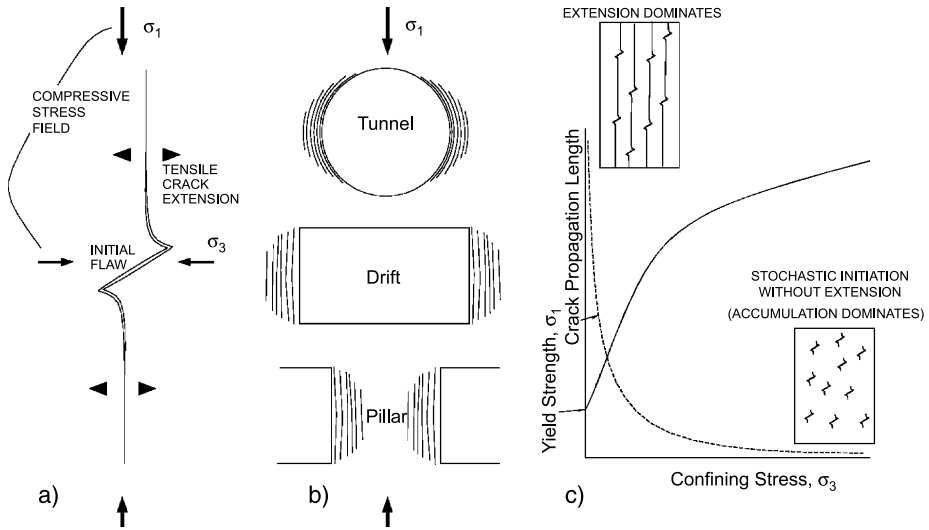
Fig. 3. Issues for stress driven instability examined in this thesis: **a**) Compression-induced tension cracking; **b**) Field-scale boundary-parallel spalling; **c**) Crack accumulation vs. propagation: yield strength and confinement sensitivity

approaching 1:1 is shown to exist between σ_1 (at first damage) and applied σ_3 in laboratory experimentation, model simulations and field observations of rockmass yield around openings (Martin, 1994, 1997). Experience (e.g. Pelli et al., 1991; Martin et al., 1999; Castro et al., 1996) has shown that the in situ strength of the rockmass near excavations in massive to moderately jointed granitoid rock consistently falls to a lower bound ($\sigma_1 - \sigma_3 = 0.35$ to $0.45\ UCS_{lab}$), coincident with the damage initiation threshold for intact rock samples (Fig. 4). Other rock types have similar ratios between 0.3 and 0.6 (as in Brace et al., 1966; Martin 1994; Eberhardt et al., 1998 and Fonseka et al., 1985, for example). A primary goal of this work is to explain this observation through a detailed examination of the damage process.

Damage initiation, accumulation and interaction are shown to be predictable processes controlled by material properties. These are primarily tensile processes; with shear mechanisms becoming important only after sufficient tensile damage accumulation and interaction has occurred. While crack initiation is only marginally sensitive to confining stress, crack propagation, a requisite process for macroscopic spalling, is highly sensitive to the low confinement conditions (as in Hoek, 1968) near an excavation boundary (Fig. 3c). In such environments, this results in a reduction in in situ yield strength, ultimately to a lower bound defined by damage initiation.

In addition to observational and empirical evidence, numerical experimentation based on simple behavioural analogues was employed in this work to illuminate key aspects of tensile strength and relaxation. A semi-analytical voussoir model (Fig. 5a) for a jointed beam, corroborated using a discrete element simulation, was modified to account for interlaminate tensile strength and for abutment relaxation. It was then applied to the study of structurally controlled instability around tunnels and underground mining stopes. A bonded disc contact model (Fig. 5b) was used to explore
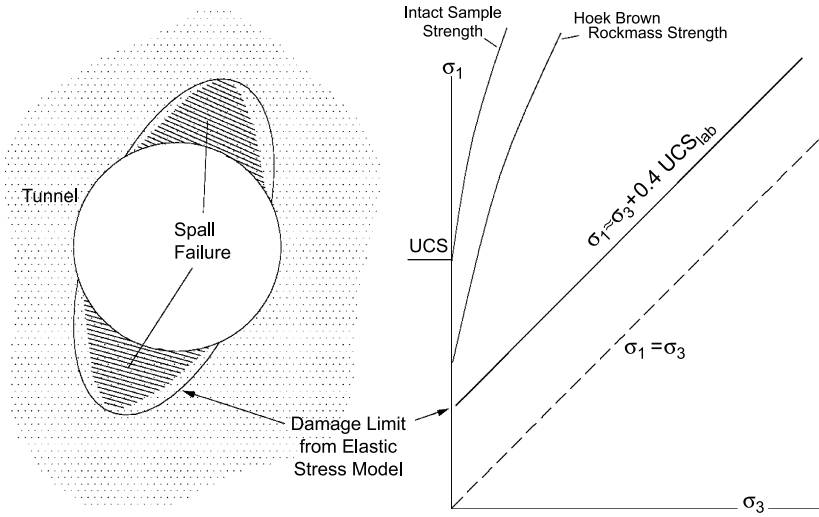
Fig. 4. Empirical threshold for in situ damage in moderately jointed hard rockmasses
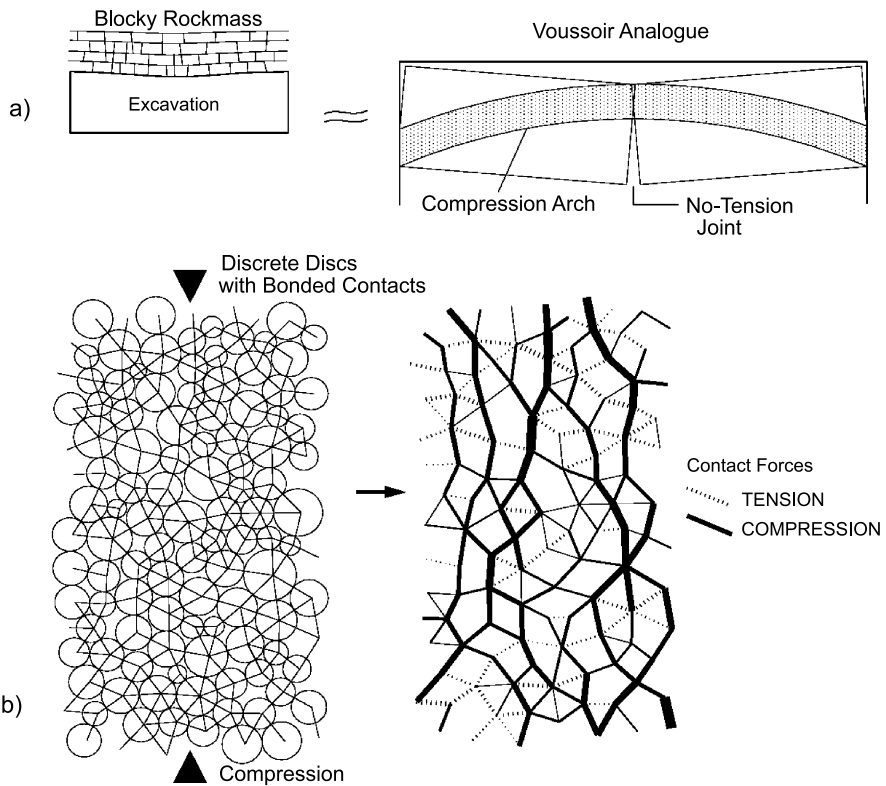
Fig. 5. Behavioural analogues: **a**) voussoir beam; **b**) bonded contact discrete elements

aspects of grain-scale tensile damage accumulation under both macroscopically tensile and compressive conditions. Other investigative tools were used in this work to complement these analogues including case study and laboratory test evidence, analytical relationships based on fracture mechanics, and a new statistical model developed herein for damage accumulation. In both structurally controlled and stress driven failure environments, the influence of tensile damage and relaxation have been quantified and used to explain observed behaviour and validate empirically based design guidelines.

2. Structurally Controlled Gravity Driven Modes

2.1 Rockmass Residual Tensile Capacity

A primary function of artificial rock reinforcement is to retain the rock's self-supporting capacity. If shear strain is dominating the rock mass behaviour, reinforcement can improve the self-supporting capacity by maintaining interlock and by suppressing dilation. In highly stressed rock, fractures form from nucleation cracks and flaws, creating surface-parallel fractures. While crack initiation is a small strain phenomenon, relatively insensitive to confinement, significant rock mass degradation as a result of fracture propagation can be effectively arrested by stiff reinforcement components that prevent the opening of fractures.

Stiff reinforcement can also preserve rock bridges formed by incomplete joint plane formation. Joints are often assumed to be fully persistent for stability analyses even though this is normally not the case in moderately jointed rock masses. Joints are often finite in dimension or are punctuated by bridges of incomplete separation. Where these rock bridges exist and where they can be preserved by careful blasting and the use of stiff tendon reinforcement, the self-supporting capacity of the rock mass, through these rock bridges, can be quite significant under tensile loading as shown in Fig. 6. These values for rock mass tensile strength were calculated using a fracture mechanics approach modified here after Kemeny and Cook (1987) as illustrated in Fig. 7 and detailed in Appendix I.

A detailed comparison of residual tensile capacity to conventional support systems is given in Table 1 based on a gravity loaded mass such as the non-sliding wedge shown in Fig. 1a. Of particular interest here is the very small relative area of rock bridging required to provide capacity equivalent to practical support systems. Note that a 1% intact rock bridge area corresponds to a 10 cm by 10 cm intact bridge within a 1 m by 1 m joint plane. For the 2D (prismatic) wedge in Fig. 1 above a 10 m span, a standard pattern of rebar reinforcement will not support the wedge (factor of safety, fos < 1) while rock bridges accounting for less than 0.5% of the joint plane (99.5% fracture development) will be sufficient to support the wedge (factor of safety = 1.1).

For the simplest of three-dimensional joint distribution assumptions (rectangular islands on rectangular joint surfaces), an observed linear joint trace persistence of 90% corresponds to a relative intact area of 1%. That is, if careful joint trace mapping in the roof of an excavation reveals joint traces 90 cm long with collinear 10 cm intact intervals, the residual tensile capacity of the rockmass normal to this joint set can be estimated to be just slightly less than that of a standard double strand cablebolt
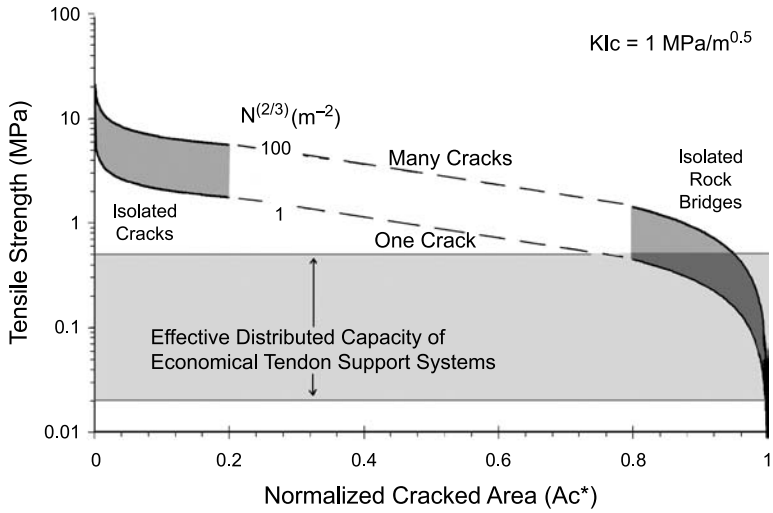
Fig. 6. a) Reduction in rock tensile strength due to isolated cracks and residual tensile capacity due to rock bridges. Compare residual strength for 90% cracked area (10% rock bridges) with average distributed capacity of conventional support systems. Left and right extremes are calculated using the respective models in Fig. 7 using fracture properties for granite. See Appendix I for details
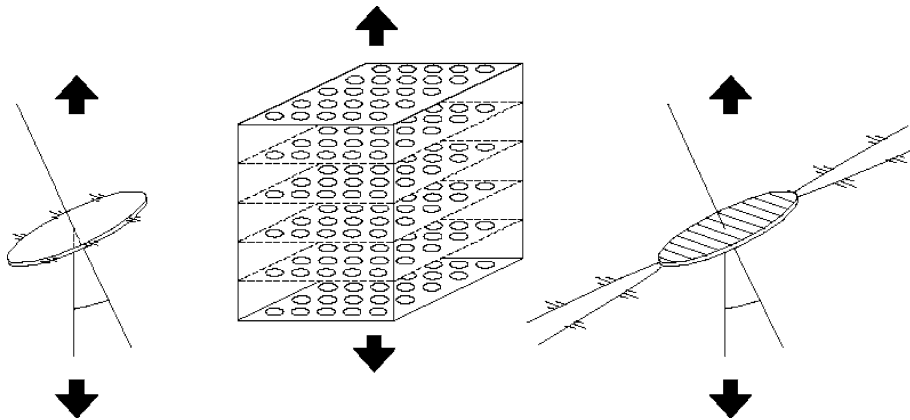
Fig. 7. Schematic of crack (left) and rock bridge (right) models used to generate Fig. 6 and Table 1

Table 1. Support patterns (capacities from Stillborg, 1994) and equivalent rock bridge area (effective residual tensile capacity)

Support type	Support pattern mxm	Equivalent pressure	Maximum supported thickness	Capacity equivalent rock bridge area (% cross section)
Rockbolts	2 × 2	20 kPa	0.7 m	0.1%
Rebar	1.3 × 1.3	60 kPa	2.0 m	0.4%
Double Strand Cablebolts	2 × 2	130 kPa	4.3 m	1.2%
Double Strand Cablebolts	1.3 × 1.3	300 kPa	10 m	4.0%
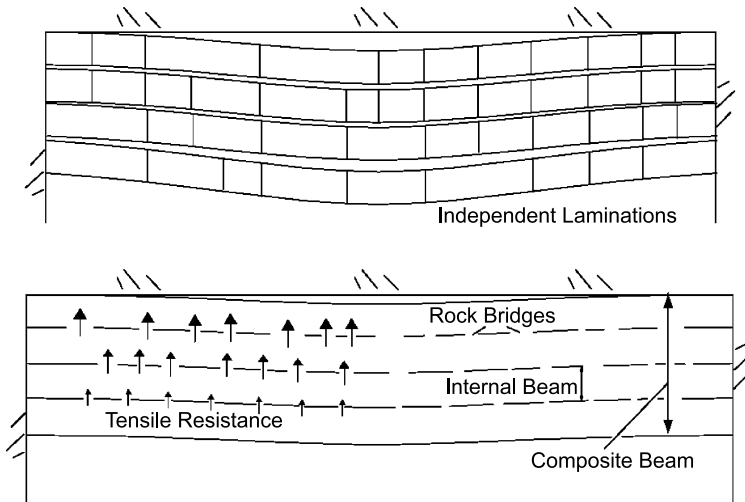
Fig. 8. Independent voussoir beams (left); beam ''stacking'' due to rock bridge tensile strength (right)

pattern (2 × 2 m). If the degree of joint development (fracture persistence) could be accurately evaluated, this would lead to significant reduction in short term support requirements for mine development and tunnelling, facilitating optimized excavation/support cycling and more rapid advance. In a dynamic environment, of course, these rock bridges cannot be considered for long term natural support as humidity and load cycling effects will lead to further propagation and rock bridge reduction. For primary, at-the-face support, however, these findings have real economic value.

Another demonstration of the impact of rock bridges and residual joint-tensile strength involves the voussoir analogue for a jointed beam or more generally a blocky, regularly jointed rockmass adjacent to an excavation as shown in Fig. 8. The original voussoir formulations of Evans (1941), Beer and Meek (1982), Brady and Brown (1993) have been updated with further enhancements and modifications developed in this work. The quantitative results in Fig. 9 are obtained by incorporating the influence of interlaminate strength into an iterative voussoir beam model.

In this analogue the rock beam cannot carry lateral tensile stresses due to beam-normal jointing. As a result the standard elastic beam formulation (as in Obert and Duvall, 1966) is not valid. The voussoir solution iteratively solves for moment balance based on a compression arch of initially unknown thickness, stress magnitude and deflection. The general voussoir solution is described in detail in Diederichs and Kaiser, 1999a (and summarized in Appendix II).

Rock bridge internal support is accounted for by relating the minimum support pressure or distributed capacity required to couple adjacent voussoir roof laminations together into a composite voussoir beam. Increased rock bridge capacity results in a thicker composite beam which enhances stability as a higher order relationship (compared to support pressure alone). Figure 9 is generalized to be independent of initial lamination thickness.
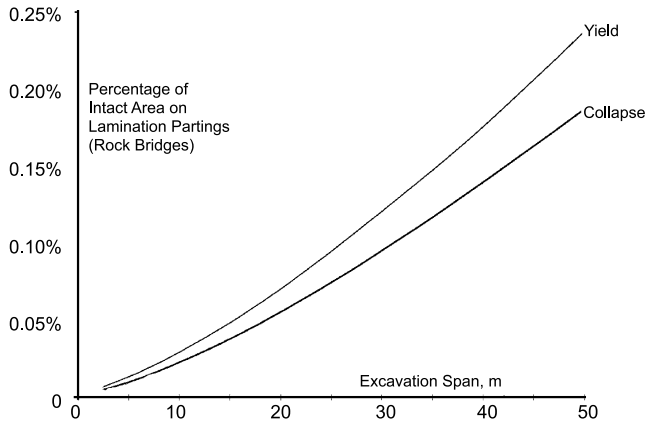
Fig. 9. Impact of residual rock bridges (as in Fig. 8) on critical span for blocky rockmasses based on modified voussoir analogue (fractured granite, rockmass modulus = 10 GPa). Lamination thickness here is assumed to be minimal (actual thickness would limit lower bound)

These rock bridges, while unstable under sustained tensile load beyond the critical levels, can yield in a stable fashion if the tensile strains are controlled (Ingraffea, 1987). A stiff reinforcement normal to these bridges acts to limit the propagation of the fractures and the rupture of the rock bridges. It is prudent to include stiff, fully coupled reinforcement components such as resin-grouted rebar in a composite support system. Even if a rebar breaks in discrete locations along the shaft, the remaining segments continue to act to suppress shear localization and to preserve rock bridges, lessening the demand on the holding components of the support system.

The preservation of rock bridge capacity in hard rock masses is particularly important at the excavation face. If careful blasting is employed, the installation of full support can be delayed. Perhaps only a spray-on lining or a thin shotcrete layer is required for worker safety at the heading. Without the installation of stiff tendon reinforcement, the rock bridges may eventually rupture, freeing unstable wedges and laminations. In many cases, however, the installation of major reinforcement can be delayed several rounds. In a mining or tunneling environment, this allows for the simultaneous installation of permanent support along with heading development and drilling for the next round (the two crews now occupy different space in the tunnel). In a typical mine, this represents a time saving equivalent to a full crew-shift and has a significant economic impact for mine development.

2.2 Abutment Relaxation

Stress paths are often highly complex around underground mine openings, involving both elevated as well as highly reduced or even tensile stresses, often in the same location at different mining stages. High compressive stress is normally associated with a higher potential for failure of underground openings as evidenced by the consideration of high stress in conventional empirical design tools. Local stress reduction or relaxation, however, can occur both normal and tangential to excavation
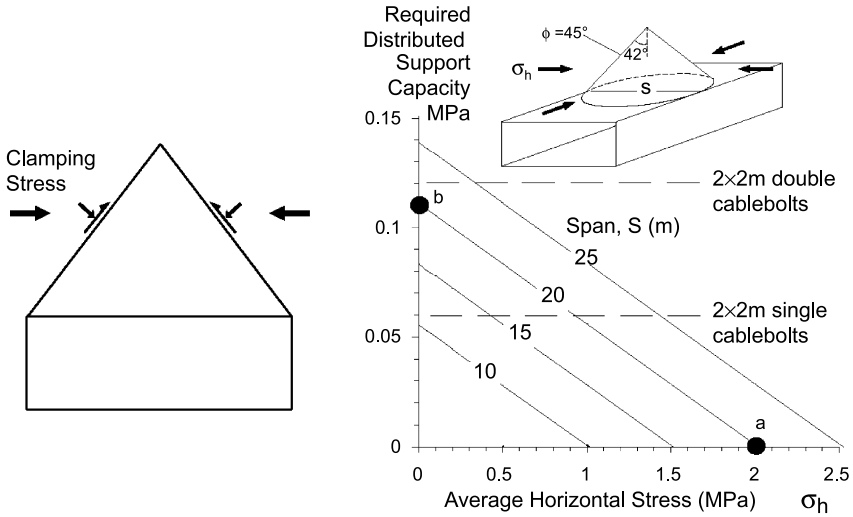
Fig. 10. Relaxation of surface parallel confinement, resulting in wedge failure. Sample wedge calculation illustrating support equivalency of minimal confinement

boundaries and can significantly reduce the inherent stability of the rockmass causing failure of the excavation wall. Typical limit equilibrium calculations (e.g. for wedge stability) or empirical design techniques for the assessment of stope wall stability often neglect the impact of abutment confinement or relaxation.

Relaxation, as discussed here, refers to the removal of compressive stress in the vicinity of and in a direction parallel to the surface of an excavation wall or roof as illustrated in Fig. 10. The wedge illustrated, bounded by continuous joint surfaces, is typically assumed to be free falling. At depth in conditions such those found in the Canadian Shield, horizontal compressive stresses flowing around this isolated excavation generate frictional strength on the joint surfaces. The relaxation or removal of this clamping stress, due to subsequent mining of nearby stopes, for example, will cause the delayed failure of this wedge, if deadload support is not provided.

In the right-hand example in Fig. 10, the increase in support pressure (distributed support capacity) required to replace the loss of relatively minor confinement for an example wedge (20 m span) is quantified:

$$F.S. = \frac{\frac{\pi \sigma_h S^2}{4 \tan \alpha} \left(\frac{K_s \cos^2 \alpha + K_n \sin^2 \alpha}{K_s \cos \alpha \cos \phi + K_n \sin \alpha \sin \phi} \right) \sin(\phi - \alpha) + F}{\gamma \frac{\pi S^3}{24 \tan \alpha}}, \tag{1}$$

where S is the span, γ is the rock unit weight, K_n, K_s are the joint normal, shear stiffnesses (normally assume $K_n \gg K_s$ or simplicity), α is the half cone angle, σ_h is the average horizontal stress across the wedge, ϕ is the joint friction angle and F is the total bolt load. It can be seen in this example that for the wedge in question, a minimum lateral confining stress of 2 MPa, acting across the back of the drift, is required for stability. This minimal excavation stress is present even at depths of less than 100 m. If relaxation (confinement loss) occurs, however, as a result of geometry
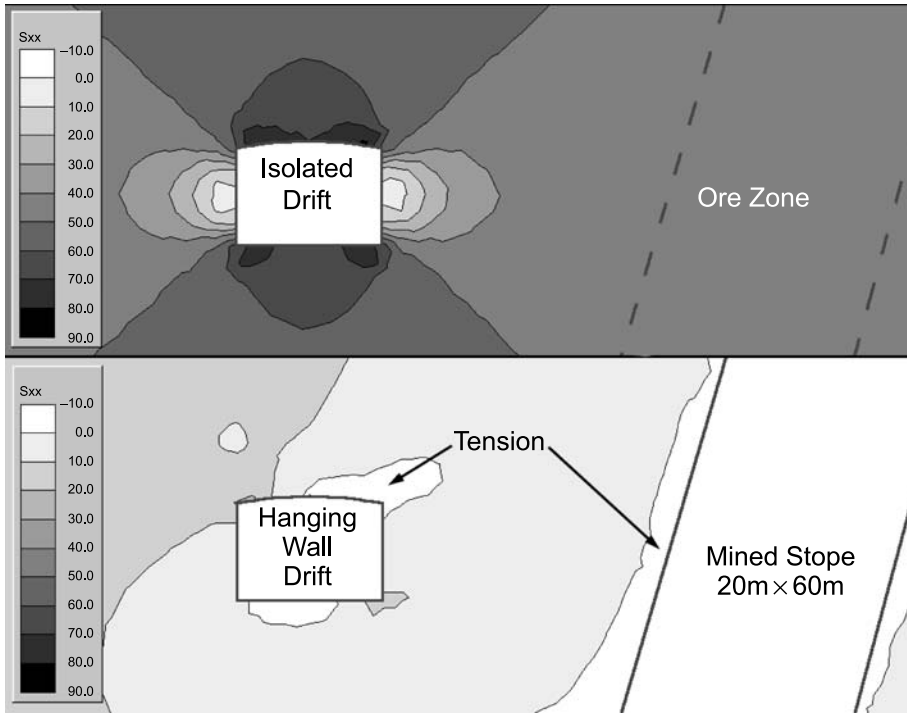
Fig. 11. Horizontal stresses above 6 × 4 m drift before (top) and after (bottom) mining of adjacent stope. Mining of the stope causes a drop in tangential stress, above the drift roof, from 80 MPa to −5 MPa. This calculated tension (elastic) would manifest as open joints and block/wedge unravelling. (In situ vertical stress 25 MPa; horizontal stress 50 MPa)

changes due to nearby mining, (as in Fig. 11), this wedge requires a heavy support system approximately equivalent to a standard pattern of double strand cablebolts.

From a practical perspective, it is necessary to be aware of this relaxation/ confinement effect so that support systems can be economized where clamping is available and enhanced where relaxation is expected. This selective approach leads immediately to significant cost reductions (less standard support) and greater safety (more support where needed).

Data collected from mine sites in Sudbury (Hutchinson, 1998) indicates that support requirements in isolated and stable mine drifts (i.e. removed from mining blocks or complex geometries) are significantly less than that predicted by a typical ubiquitous joint and wedge or beam analysis. On the other hand these steeper wedges can still be present and are likely to be released if clamping stresses are reduced. Likewise, blocky rockmasses are more likely to unravel in these areas. Stope access drifts and cross-cuts are particularly susceptible.

Extreme relaxation occurs when the absolute boundary-parallel strain (compression positive) drops below zero (datum at zero stress). This manifests itself as the opening of joints and is equivalent to an outward absolute displacement of the abutments or as an equivalent boundary parallel tension in an elastic stress model. In the example illustrated in Fig. 11, a previously isolated drift experiences the effects of
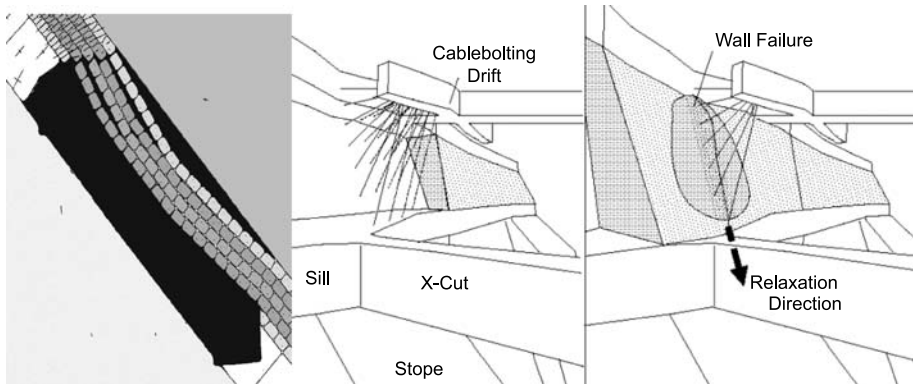
Fig. 12. Typical laminated hangingwall rockmass (voussoir) schematically simulated with discrete elements (left); cablebolt array in hangingwall (Winston Lake Mine, Ontario, Canada) before and after stoping advance (right). Abutment relaxation due to increased deformation into cross-cuts ("x-cut") lead directly to wall failure (modified after Diederichs and Kaiser, 1999a)

nearby mining. One effect of the stope is to reduce the horizontal stresses in the back of the drift (to tensile values in this elastic example).

The complexity of typical ore zones and the operational constraints inherent in mining often result in groupings of multiple openings favouring the creation of relaxation zones. Blocky rockmasses within these zones are subject to unraveling or structural collapse. In addition to safety concerns, this failure leads to production delays (due to oversized muck) and to costly dilution. Stope geometry and operational decisions can also lead to abutment relaxation and hangingwall failure as shown in Fig. 12. In this example the advancing stope is oriented, with respect to in situ stress, such that hangingwall confinement is reduced. Coupled to this is the creation of a cross-cut to the bottomsill which locally increases the downward displacement of the lower hangingwall abutment. The combined effect results in the failure illustrated. Discrete element simulations showed that the hangingwall was indeed stable until the lower abutment was softened to simulate the creation of the cross-cut. Aspects of this case study are described by Diederichs and Kaiser (1999a, b) and also by Maloney and Kaiser (1991) and Kaiser et al. (2001).

In order to quantify this effect and incorporate relaxation into existing design tools, the voussoir beam analogue presented by numerous authors in the past was updated and modified to account for abutment relaxation. Extreme relaxation, equivalent to boundary-parallel tensile stresses in an elastic model, can be represented as the outward displacement of the abutments, δa, as shown in Fig. 13. This results in increased beam deflection at equilibrium and smaller critical spans for a given beam thickness, T, and rockmass modulus, E_{rm}. Using the modified voussoir model developed here, this effect is demonstrated in Fig. 14.

In order to apply this new analogue to design, the Modified Stability Graph, now in common use in Canadian mining for stope dimensioning, is further adapted for relaxation. The original technique has been well documented in the literature (Bawden, 1993; Diederichs and Kaiser, 1999b; Potvin and Milne, 1992; Hutchinson and Diederichs, 1996; etc.). The method compares the ratio of stope face area/perimeter
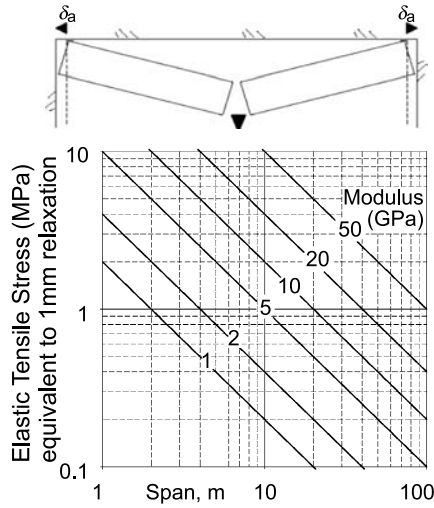
Fig. 13. Elastic tension (continuum model) equivalent to 1 mm of outward abutment displacement due to relaxation (modified after Diederichs and Kaiser, 1999a)
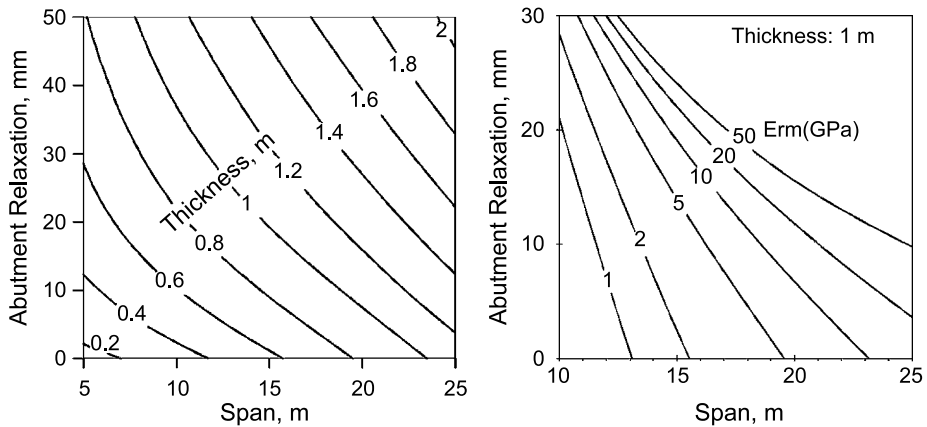
Fig. 14. Reduction in critical unsupported span due to relaxation for rockmass modulus $E_{rm} = 10\,\text{GPa}$. (left) and lamination thickness, $T = 1\,\text{m}$

("hydraulic radius") to a rockmass stability number N, a direct product of the factors: 'RQD/Jn' (block size); 'Jr/Ja' (joint surface condition); factor 'A' accounting for induced compressive stress/strength; factor 'B' accounting for joint-face interaction angle and 'C', a factor accounting for face and structure inclinations with respect to gravity. The first two terms are directly from the Q system (Barton et al., 1974) while the others are summarized in the literature previously listed (e.g. Bawden, 1993). Factor A is of particular importance here and is illustrated in Fig. 15. This factor considers only the increase in compression tangent to the stope wall and does not
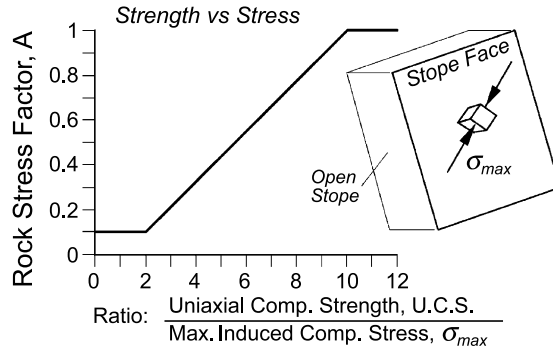
Fig. 15. The relative stress factor included in the Modified Stability Number, N' (after Hutchinson and Diederichs, 1996)
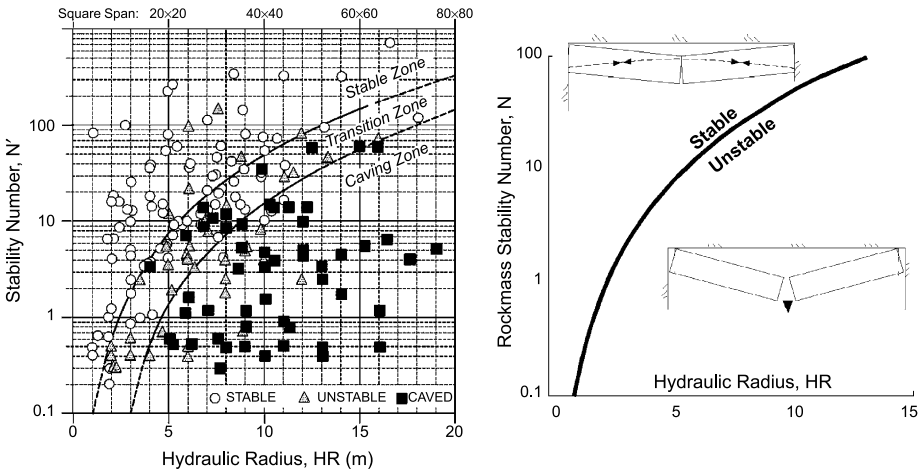
Fig. 16. a) Unsupported stope database and resultant no-support limit for Modified Stability Chart (data from Potvin, 1988 and Nickson, 1992); **b)** Calibration of voussoir model (relating key model parameters to N'). *HR* is directly related to nominal span

include the effects of relaxation. The final no-support stability limit (upper bound in this case) in Fig. 16a is the result of calibration based on the original database of unsupported stopes by Potvin (1988).

An interpretation of the voussoir analogue with respect to the no-support limit is shown in Fig. 16b. Here the model is assumed to have near-rigid abutments. The voussoir model developed here is calibrated with respect to rockmass factor N' (result of rockmass classification, stress and joint factors) and stope geometry factor, *HR*, using a multi-parametric procedure described in Diederichs and Kaiser, 1999a. Above the no-support limit the voussoir beam model is stable. Below the limit, the beam model is adjusted so as to fail (Fig. 16b).

Now the effect of abutment relaxation can be assessed and the impact on the empirical no-support limit can be estimated (recall that the factor A for stress effect
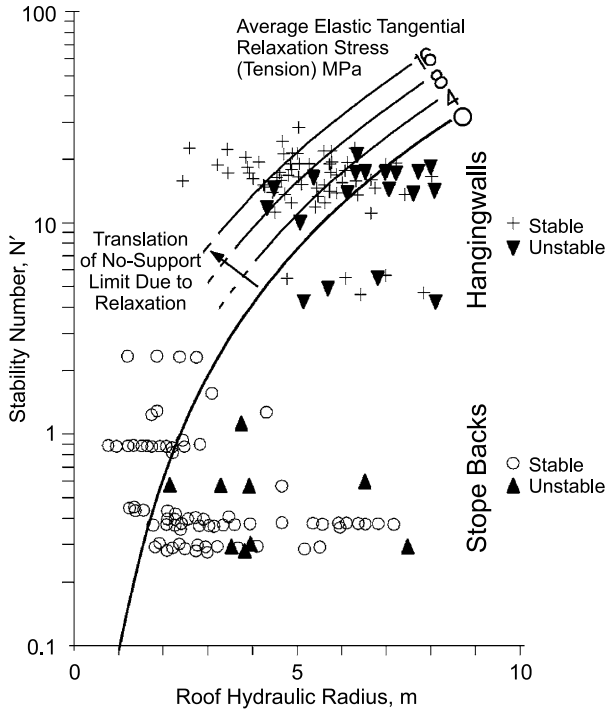
Fig. 17. Adjusted no-support limits for Stability Graph based on relaxed stope walls. Data points show independent verification case histories. Backs are in compression while hangingwalls are relaxed

does not consider loss of confinement or elastically calculated tensile stress). Using this calibrated model and the relationship between abutment displacement and calculated elastic tensile stress in Fig. 13, the revised no-support limits shown in Fig. 17 are obtained.

The data points in Fig. 17 represent an independent verification set based on documented case histories from Bawden (1993) and from (Greer, 1989). The hangingwalls in question were relaxed (showing nominal tensile stress in a 3-dimensional elastic model) while the stope backs were under compression. The original no-support limit does not accommodate this relaxation. The revised no-support limits (calculated according to the equivalent relaxation stress) show a considerable predictive improvement. The relaxation adjustment is integrated into the N' factor (through a modified stress factor, A) for future design:

$$A = 0.9e^{11\left(\frac{\sigma_T - \sigma_0}{UCS}\right)} \quad \text{for } \sigma_T < 0, \tag{2}$$

where σ_T is the minimum tangential stress and σ_0 is an offset term normally set to zero. In this relationship, the definition of tension may require adjustment due to the accuracy of elastic models in the near-zero stress region. Experience with three-dimensional direct boundary element formulations (linear elements) has shown that modelled stresses up to 5 MPa (positive compression) can be indicative of zero stress

or tension. For these analyses set σ_0 to a positive offset between 0 to 5 MPa. Simple trial experimentation is recommended for any numerical scheme prior to design application.

In addition to the effects of relaxation on rockmass integrity, the effects on support performance can also be compromised as in the case of plain strand cablebolts and other frictional support systems. The reader is referred to Hutchinson and Diederichs (1996), and Kaiser et al. (1992) for detailed discussions of this problem.

The examples presented here highlight the importance of abutment relaxation as a destabilizing mechanism. An understanding of this mechanism enables the engineer to optimize mine sequencing and stope geometries to preserve clamping as well as to use more discretion in support specifications for isolated drifts and for near-stope accesses, thereby increasing development economy and safety. Using a calibrated voussoir beam approach, the empirical stability graph for stope design has been updated to account for relaxation across stope backs.

The importance of both tensile damage mechanics and confinement reduction have been clearly demonstrated for the regime of structural instability. A survey of reportable incidents in hard rock mines in Sudbury (Hutchinson, 1998), indicated that structural failure accounted for approximately 70% of reported incidents (in access drifts) in hard rock mines in the Sudbury area. Many of these occur in near-mining zones where relaxation is dominant. These reportable incidents refer to falls some time after the initial development (groundfalls at the development face were not counted unless extremely severe). It can be assumed then that stable or subcritical fracture propagation (as in Atkinson and Meredith, 1987) or dynamic fatigue leading to rock bridge degradation may have played a part in some of these failures. The prudent response to these incidents is to increase standard support for all development. Clearly this is a needless expense if the mechanisms of failure (relaxation and rock bridge destruction) are not prevalent, as in major isolated development away from active mining. An appreciation of these mechanisms leads directly to support optimization in such cases.

3. Stress Driven Damage and Failure Modes

In combination, tensile damage and confinement reduction also play important roles in the stress-induced yield of hard rock at depth. Tensile micro-cracking, exacerbated by low confinement conditions near excavations, leads to a unique failure process (slabbing in the extreme) that is inconsistent with conventional shear based failure criteria. Rock mass strength near underground excavations is controlled by damage initiation mechanisms that are relatively insensitive to confinement and by fracture propagation (extension) mechanisms that dominate at low confinement. For brittle rock, the strength envelope can be represented by a multiphase linear failure envelope illustrated in Fig. 18. This envelope will be shown to be the result of the mechanics of tensile fracture accumulation and propagation and the reduction of the yield surface to the damage initiation threshold as confining stresses are relaxed.

Below the ''damage initiation threshold'' the rock is not damaged and remains undisturbed. When this threshold is exceeded, seismicity (acoustic emissions) is
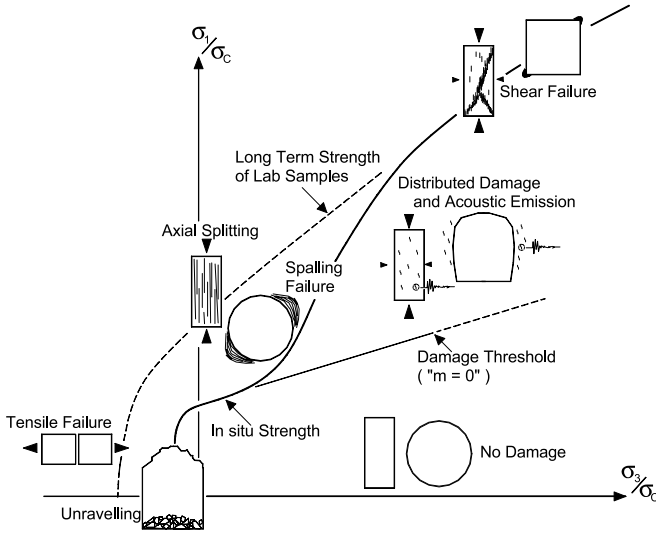
Fig. 18. Schematic of failure envelope for brittle failure, showing four zones of distinct rock mass failure mechanisms: no damage, shear failure, spalling, and unraveling. σ_c is the unconfined compressive strength (UCS) of laboratory samples

observed and micro-crack damage accumulates, leading to a critical crack intensity for crack interaction and coalescence resulting in macro-scale shear failure if the confinement level is sufficiently high (e.g., in confined cylindrical test samples). When a stress path moves to the left of the low confinement zone, (into the zone marked "spalling failure" in Fig. 18), and exceeds the damage initiation threshold, individual cracks can propagate beyond grain boundaries leading to macroscopic axial splitting or spalling normal to the minor principal stress. As a result, the observed in situ rock mass failure stress is significantly lower than predicted from laboratory tests as fewer cracks are required for yield. In cylindrical lab samples under axisymmetric compression, spalling failure is retarded due to the geometric constraints and the theoretical yield strength ("long term strength") is achieved with some additional system dependant strain-hardening up to peak (not shown in Fig. 18). This will be discussed further in the following sections.

3.1 Bounding Limits for In Situ Strength

The lower bound in situ threshold for damage, discussed in Section 3.2, is defined by the limit for damage initiation in laboratory samples. For example, Hommand-Etienne et al. (1995) showed that the criterion for damage initiation in Lac du Bonnet granite was approximately:

$$\sigma_{1initiation} \approx A \cdot UCS + B\sigma_3, \tag{3}$$

where $A = 0.33$ and $B = 1.5$. Brace et al., 1966, showed a similar relationship for Westerley Granite with a $A = 0.3$ and $B = 1.4$ while Pestman and Munster (1996)
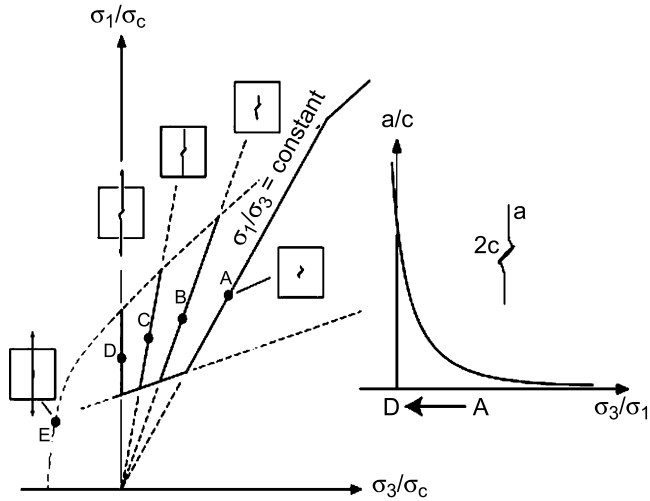
Fig. 19. Increase in crack propagation with reduced confining stress. Tensile stresses lead immediately to unstable propagation and spalling. Low confinement encountered in near-excavation domains leads to spalling and strength reduction near the excavation boundary with a lower limit defined by crack initiation. (*a* is the new extending crack length while *c* is the initiating flaw or limiting grain dimension)

demonstrated a slope, *B*, of 2 for the initiation threshold (σ_1 *vs* σ_3) for sandstone. Interestingly, this is consistent with the so-called "serviceability limit" for concrete (Illston et al., 1979) which suggests a design limit according to Eq. (3) with $A = 0.3$ and $B = 2$. Below this limit no cracks can form and no yield can occur.

It will be shown that the upper bound for in situ strength, examined in Section 3.3, is defined as the stress threshold at which non-propagating cracks (cracks which initiate but do not propagate beyond one grain dimension) accumulate to the point that crack-crack interaction is inevitable and localization ensues. This threshold corresponds to the long-term laboratory strength (as tested in Martin, 1994).

The transition between the upper bound (crack interaction) and the lower bound in situ strength (damage initiation) in Fig. 19 is controlled by the "spalling limit". This is a confinement ratio limit (σ_3/σ_1) below which uncontrolled crack propagation can occur. In other words, intragranular cracks propagate beyond the grain or crystal boundaries and become macro-cracks or spall fractures (Fig. 19). Hoek (1968) had suggested that this occurs below a ratio of approximately 0.1 to 0.05.

3.2 Field Evidence for a Lower Bound Damage Initiation Threshold

Pelli et al. (1991) showed that in order to fit the Hoek-Brown criterion to observed tunnel failures, the value of *m* had to be reduced to unconventionally low values. Martin et al. (1999) found that *m* should be close to zero for hard rock. Similar findings were reported by Castro et al. (1995) who showed, using back-analyses of brittle failure, that stress-induced fracturing around tunnels initiates at approximately 0.3 to 0.5 σ_c ($s = 0.10$ to 0.25) and that it is essentially independent of confining stress. In Diederichs (2000) additional cases were developed to illustrate this effect including
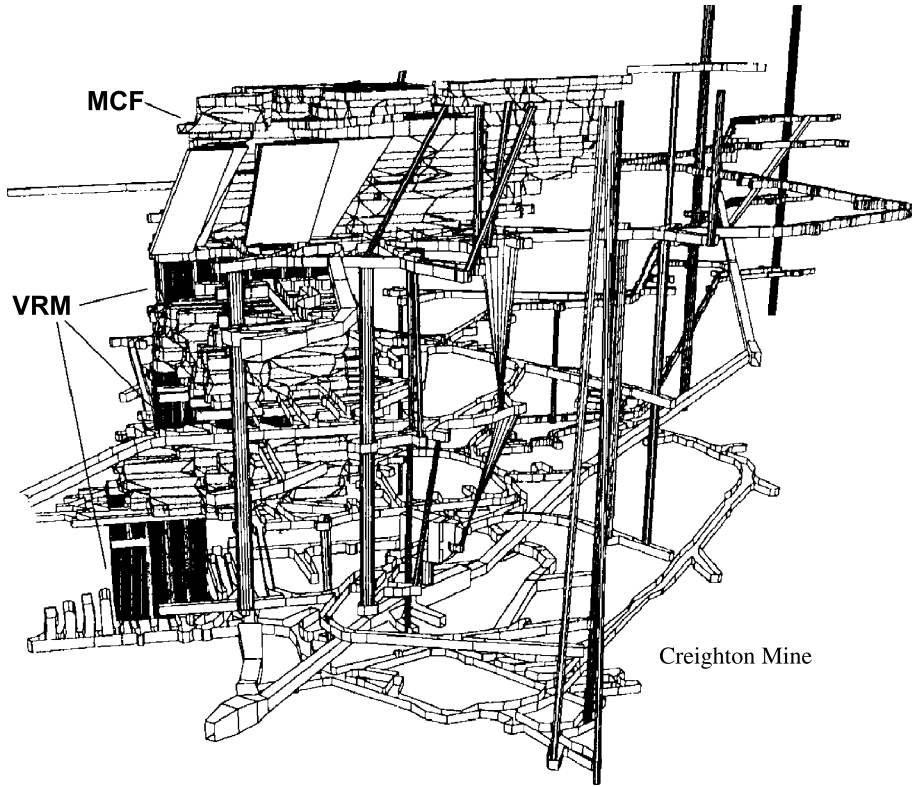
Fig. 20. Perspective view of Creighton Mine Deep Levels. The upper horizon shown is 6400 level. The upper most VRM stope block as labeled is the study area

observations at Creighton Mine in Sudbury, Canada. Creighton Mine is the largest and deepest operating nickel mine in North America. It began as an open pit operation in 1901, progressing underground using a variety of mining methods over the next 90 years. In the deep levels of Creighton Mine, illustrated in Fig. 20, the primary mining method up until the mid 1980's was Mechanical Cut and Fill (MCF).

It was decided in the mid 1980's to experiment with the use of the vertical retreat method, VRM, which is now routinely used throughout the Canadian mining community. This method had the advantage of removing miners from the open stope for most of the mining cycle and did not create horizontal sills. The stopes were to be mined incrementally in 13 m square panels. Ultimately these panels would be mined full height (65 m). During the trial documented here, however, the panels would be mined vertically between the topsill and the top of the uppermost MCF horizon as shown in Fig. 21. Due to the geometric complexities, stresses are calculated with a 3-Dimensional elastic boundary element model (Map3D – Wiles 1996) of the full Creighton Deep Zone.

In situ stresses (linearly varying with depth) at the 6700 level are $\sigma_1 = 82$ MPa, $\sigma_2 = 62$ MPa, and $\sigma_3 = 53$ MPa. σ_1 is horizontal and approximately east west, while σ_3
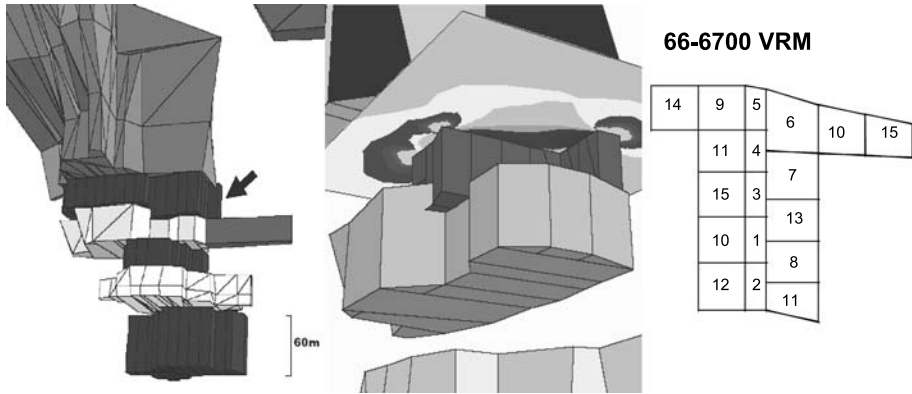
Fig. 21. Left: Map3D model geometry for completed MCF and VRM stopes for Creighton deep (to 7200 ft level). Arrow shows the 6600–6700 VRM block. Middle: Major principal stress around the completed 66–6700 VRM (West). Right: Stope extraction sequence for study block (plan view)

is vertical (in the absence of mining). The stopes in figure were monitored (as in Landriault and Oliver, 1992) using an extensive cluster of extensometers, stress cells and borehole camera devices. The borehole camera information was used in combination with drilling logs (fines, ease of drilling, borehole breakout or visible closure, stuck rods, etc.) from the blastholes in neighbouring panels to delineate the extent of the damaged or yielded zone. Zones of actual observed yielding are shown for three mining stages in Fig. 22.

In this study, for each simulation of 3-D elastic stresses around the completed mining geometry, a grid of points was overlain in the unmined zone and was sampled, recording the calculated stress state and noting whether the point fell inside or outside the observed yielded zone. The results are shown in Fig. 23. The filled squares ("yielded") indicate points inside the observed yielded zone while the circles ("intact") represent stress points outside this zone.

The lower bound yield stress for low and moderate confinement (σ_3) follows the relationship:

$$\sigma_1 = (90 \text{ to } 100)\text{MPa} + (1.0 \text{ to } 1.2)\sigma_3, \tag{4}$$

where 95 MPa is approximately 0.4 to 0.5 times the *UCS* of the intact Creighton granite and norite respectively (250 MPa and 190 MPa as specified by Wiles, 1989). This lower-bound in situ threshold is consistent with the laboratory threshold for damage initiation. This relationship scales up in this way due to the moderately jointed character and high integrity of the rockmass (joints are tightly closed and do not impact on the rockmass strength at this scale of observation).

3.3 A Bonded Solid Analogue for Crack Accumulation and Interaction

Returning to a laboratory scale, in order to better understand the relationship between crack initiation (lower bound strength) and crack interaction (upper bound in situ strength), a discrete element simulation based on elastic bonded discs and breakable
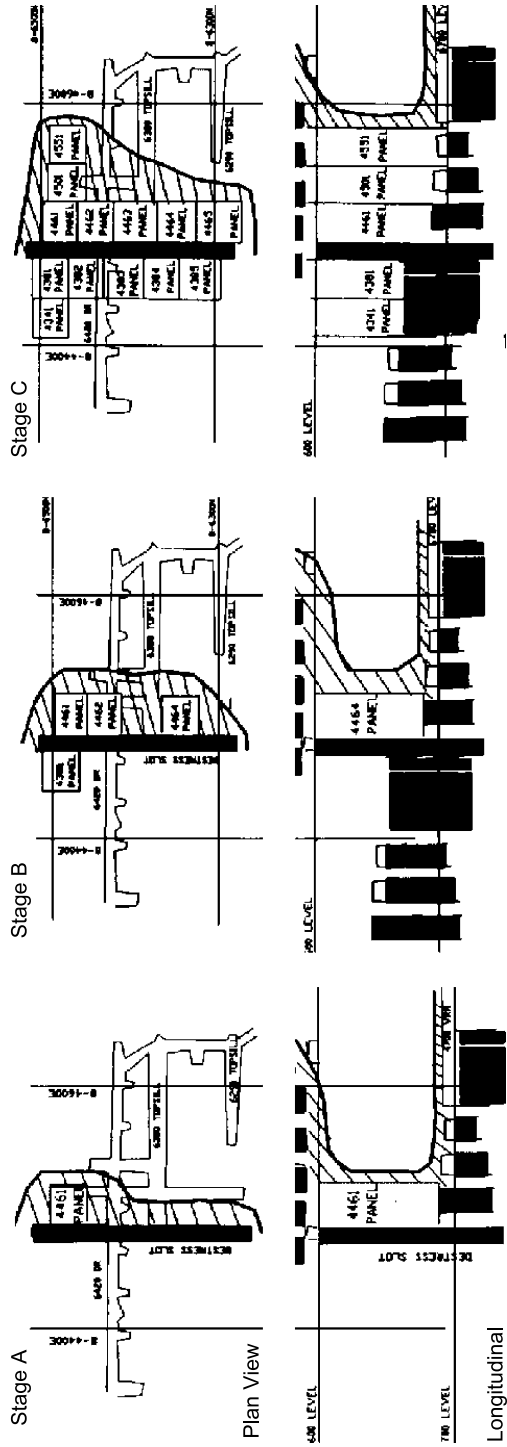
Fig. 22. Observations of yielding and damage for six excavation stages (modified after Landriault and Oliver, 1992). Hatched area represents observations of yielded ground around numbered stope panels
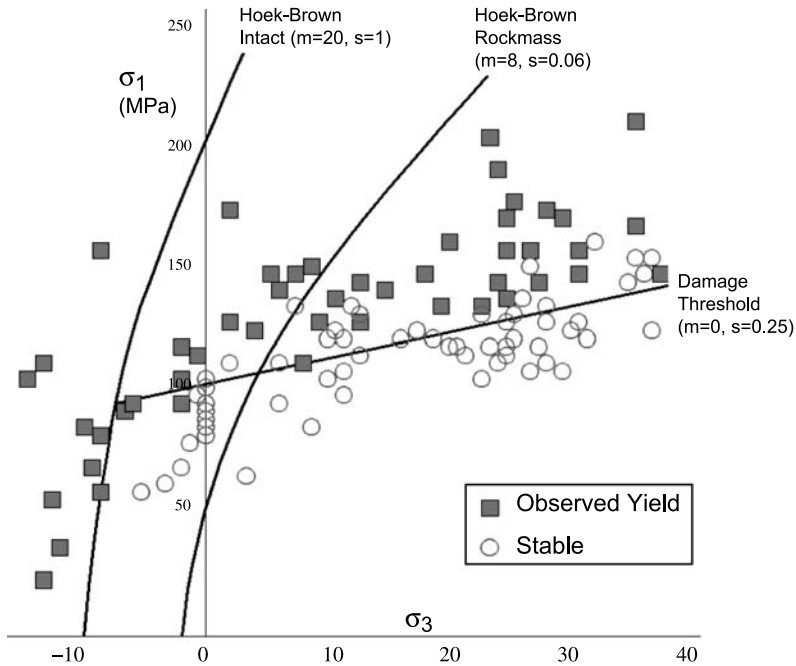
Fig. 23. Correlation between observed damage and elastic stress calculations at randomly sampled locations in the model of Fig. 21. Damage threshold (minimum major stress) corresponds to a Hoek-Brown envelope with $m = 0$

contact bonds is used to investigate damage propagation in heterogeneous solids. The model, based on the user-modifiable PFC code (Itasca, 1995) considers rock as a heterogeneous assembly of discs bonded together at contacts with elastic springs resisting interparticle shear and normal translation. As a result of heterogeneity, stresses are carried through the sample as a tortuous network of contact forces. Under confined compression, this tortuosity results in numerous contact bonds with tensile forces as well as those with compression (Fig. 24). The sample is formed by creating a random assembly of particles with varying radii and inflating the particles until maximum contact density is achieved. At this point bonds are formed and normally distributed contact stiffnesses and strengths are assigned. In a biaxial sample, wall confinement is achieved during testing with rigid walls or flexible "membranes". Simulated rigid top and bottom platens converge, resulting in increasing deviatoric stresses. When either a tensile normal-force or a shear-force limit is reached, the bonds break and cannot carry tension thereafter (frictional sliding is still resisted). Cracks accumulate as irreversibly broken bonds until sample failure occurs.

At the scale of a single crystal grain, the nominal tensile bond strength used was one quarter of the shear strength (based on results from experimental fracture mechanics by Okubo and Fukui 1996 and Laqueche et al., 1986), and therefore dominated the local damage process in unconfined and confined test simulations, even though the eventual failure mode resembled macroscopic shear (Fig. 25). A typical axial stress versus axial strain curve from these simulations is shown in Fig. 26.
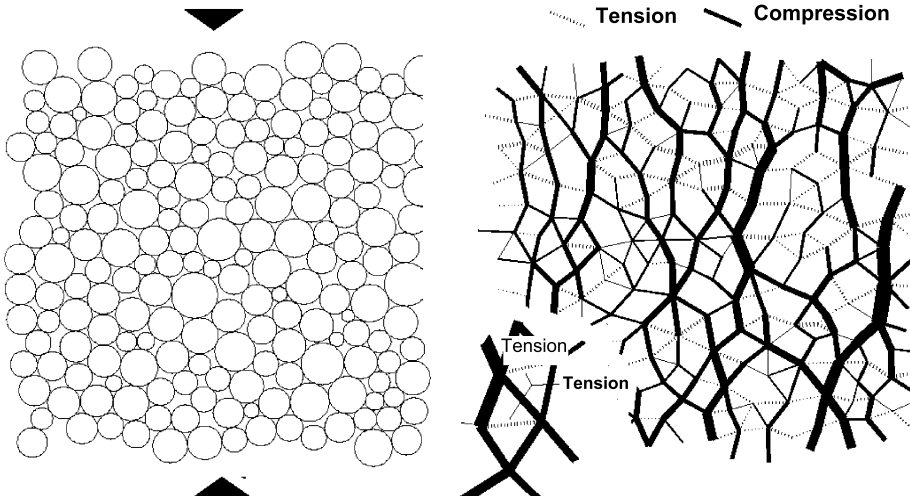
Fig. 24. Disc arrangement (simple contact bond model) and contact forces for a random assembly
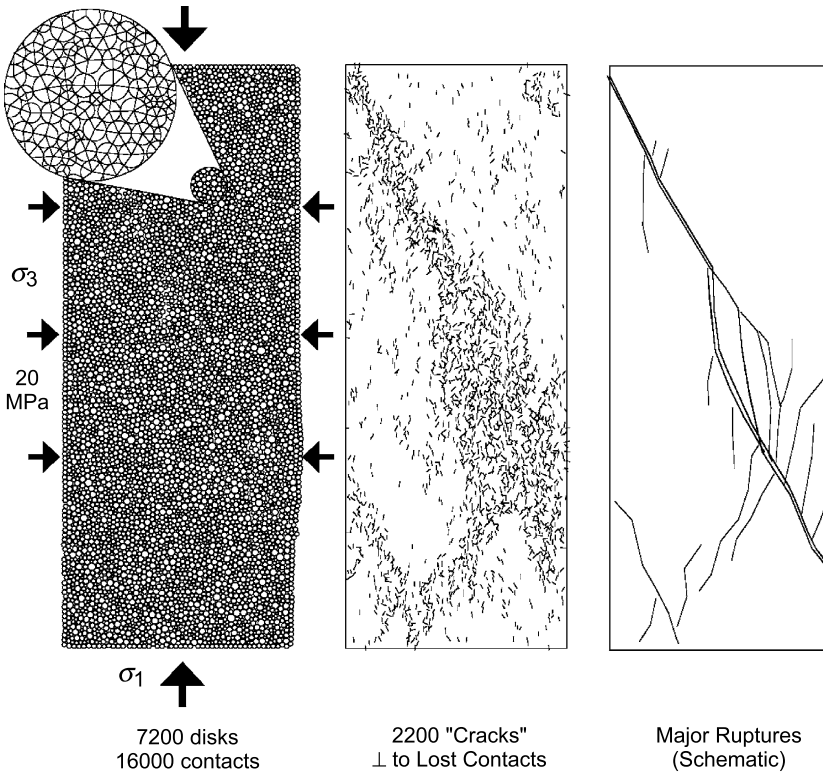
Fig. 25. Confined compression test on a bonded disc sample. Cracks show as segments normal to ruptured bond. Right-hand image is a manually generated schematic of major rupture coalescence based on individual cracks in middle figure
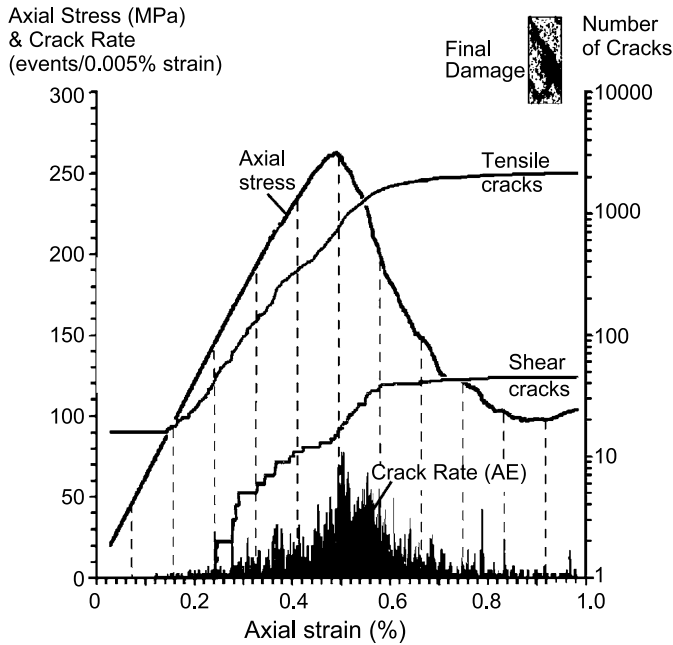
Fig. 26. Typical confined ($\sigma_3 = 20$ MPa) compression response (same sample as Fig. 25). Shear/normal strength ratio $= 4$; 7200 discs and 16000 contacts. Mean normal bond strength $= 0.3$ MN

The stress-strain curve shows the characteristic damage initiation at about 0.3 to 0.4 of the peak strength and rapid strain softening immediately after peak. Note that even though the sample is confined with 20 MPa, the total amount of tensile cracking dominates shear cracking by a ratio of approximately 50:1. In the extreme, if shear bond failure is prevented completely (only tensile bond failure allowed), coalescence of exclusively tensile cracks still results both in realistic spalling (Fig. 27b) and in shear/rotation zones reminiscent of macro-shear failure as in Figs. 27c and 27d.

Heterogeneity (both in grain size and material properties) is key in generating tensile stresses in a compressive stress field. These tensile stresses (and strains) occur, of course, within individual crystal grains, giving rise to crack initiation. Composite heterogeneity, however, also results in meso-scale tensile zones spanning numerous crystals. In these areas, crack propagation beyond the limiting grain scale is possible. A numerical simulation (bonded disc model) is used in Fig. 28 to illustrate the generation of both grain scale tension and more regional tensile stress through heterogeneity. This simulation is under applied lateral confinement (2.5 MPa) and a vertical compression of 100 MPa.

While the program PFC permits the use of more sophisticated bonding models, the bonding model used here is a simple tensile bond with no moment effects. In addition, the discretization does not permit a singular stress concentration effect as in real microcracks. As a result, grain-scale cracks do not readily propagate in isolation using this simple contact bond model. As the simulations are performed with the element size equated to the mean grain size, crack blunting caused by crystal/grain boundaries
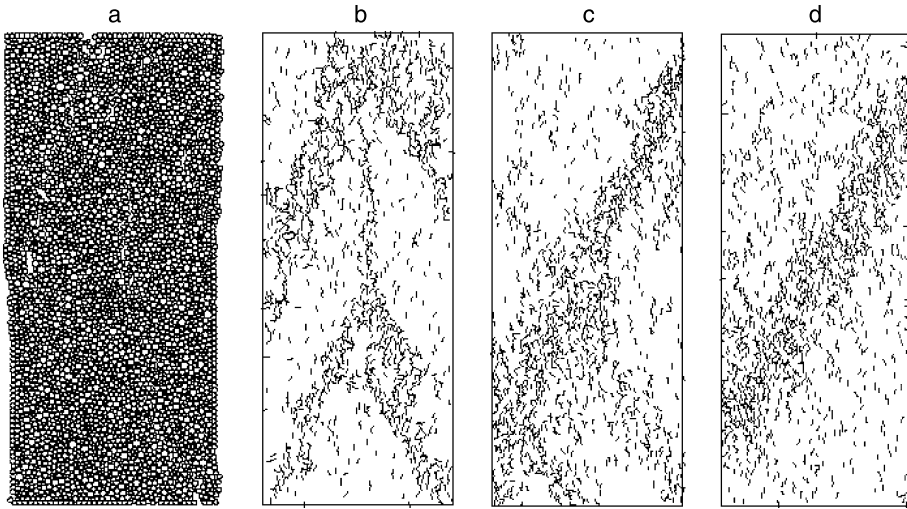
Fig. 27. Macro failure zones in discrete element model: **a**) and **b**) discs and cracks for unconfined sample; **c**) $\sigma_3 = 20\,\mathrm{MPa}$; **d**) $\sigma_3 = 60\,\mathrm{MPa}$. All micro-damage is tensile – shear bond failure is prevented. Shear zones result from tensile crack coalescence

is reflected in the model. These cracks do, however, accumulate and interact with other cracks. After the first crack initiation (bond rupture) a period of uniform accumulation of isolated cracks ensues as illustrated in Fig. 29. Once two cracks interact (i.e. initiate within proximity of each other) a meso-flaw is created, spanning two to three grain dimensions. This flaw is now large enough to spontaneously drive failure of adjacent particle bonds. Crack interaction, therefore, marks the onset of true yield in these simulated specimens.

The model is used to convincingly demonstrate that true sample yield (deviation from a non linear response) is coincident with the first crack interaction (Fig. 30). This interaction is a probabilistic phenomenon and occurs when a critical crack density is reached. After initiation cracks begin to form oblique to the maximum compression and the crack anisotropy declines as shown in Fig. 30. Furthermore, this critical crack density, the onset of stress-strain non-linearity was shown to correspond to a consistent level of lateral extension strain (Fig. 31). This is, of course, consistent with the criterion developed by Stacey (1981) for yield defined by a critical extension critical extension strain threshold (e.g. for granite: critical extension strain $\varepsilon_{cr} = 0.03\%$, $E = 60\,\mathrm{GPa}$, $v = 0.2$):

$$\sigma_1 = \frac{E}{v}\varepsilon_{cr} + \frac{1-v}{v}\sigma_3 = 72 + 4\sigma_3. \tag{5}$$

In the simple contact bond model used here, this density critical extension strain was indeed independent of confining stress and was even consistent in the tensile regime (Fig. 32). The slope of the threshold defined by Eq. (5) is approximately equivalent to a Mohr-Coulomb envelope with a friction angle of 37 degrees. The important point here is that this confinement dependency for crack interaction, and
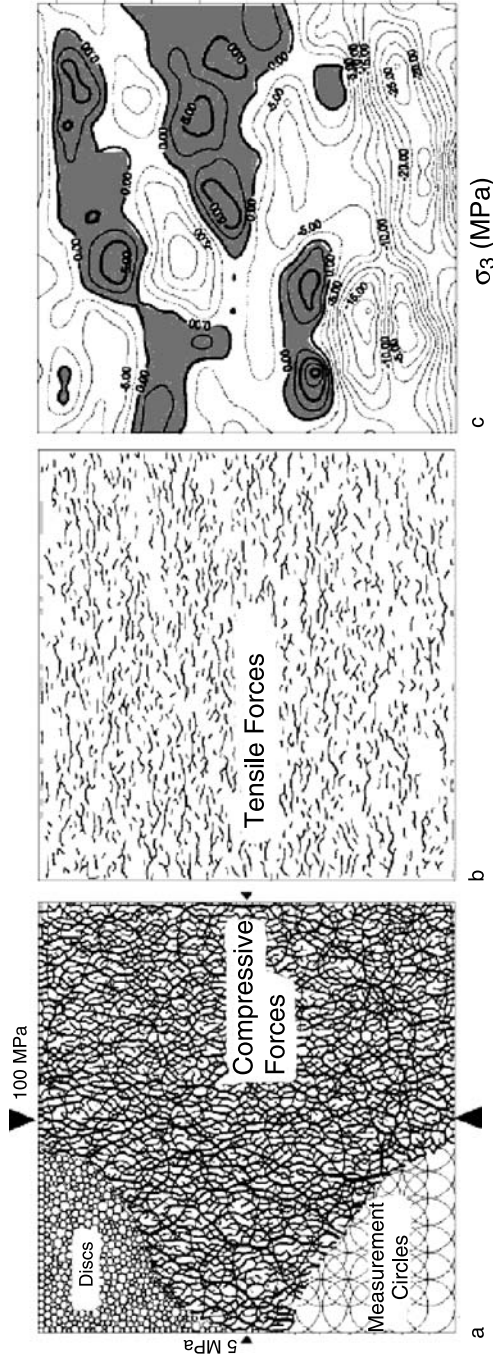
Fig. 28. A schematic assembly of discrete bonded discs under 5 MPa of confining stress and 100 MPa of axial stress. In **a**) compressive forces are shown within the contact web. Measurement circles are used to calculate average stresses within sample regions (based on contact forces). In **b**) tensile contact forces are shown. In **c**) calculated minor principal stresses are calculated using measurement circles – shaded areas represent regional tensile stresses
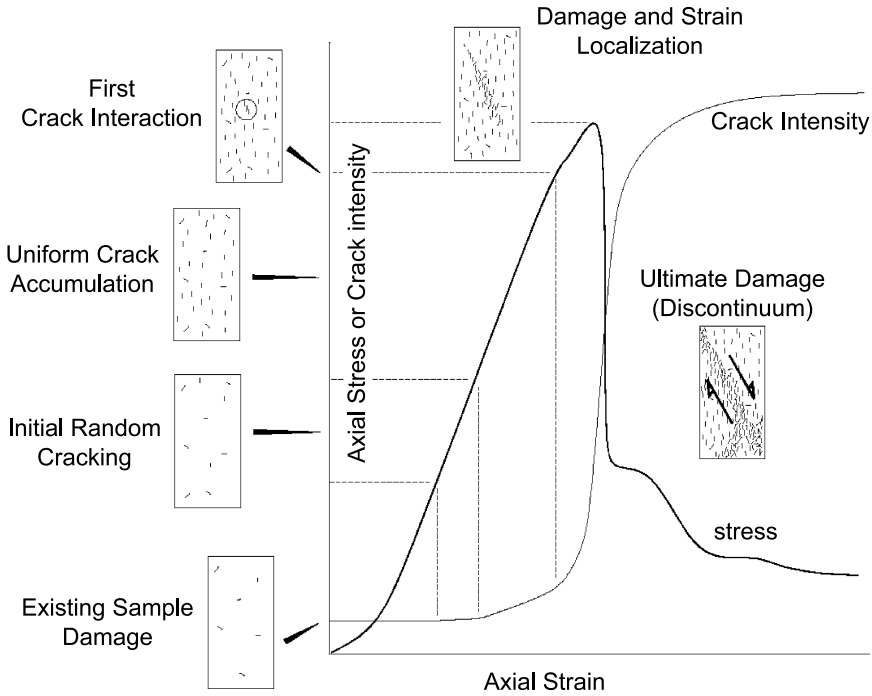
Fig. 29. Stages of damage within bonded disc model – representative of actual laboratory test sample
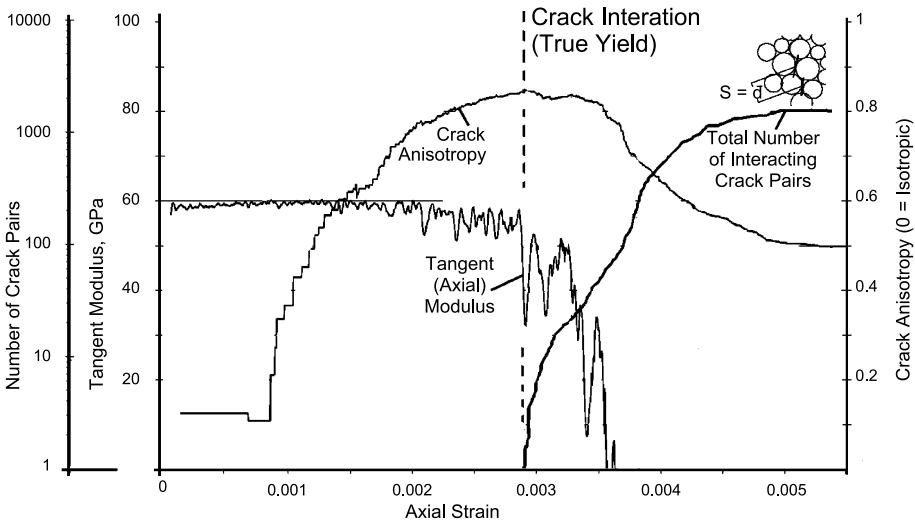
Fig. 30. Crack interaction indicated by rapid accumulation of neighbouring crack pairs (separation S is equal to or less than grain diameter d), axial non-linearity (drop in tangent modulus and peak anisotropy, α (normalized second invariant of crack tensor: $\alpha = 0$ for isotropy, $\alpha = 1$ for parallel cracks)
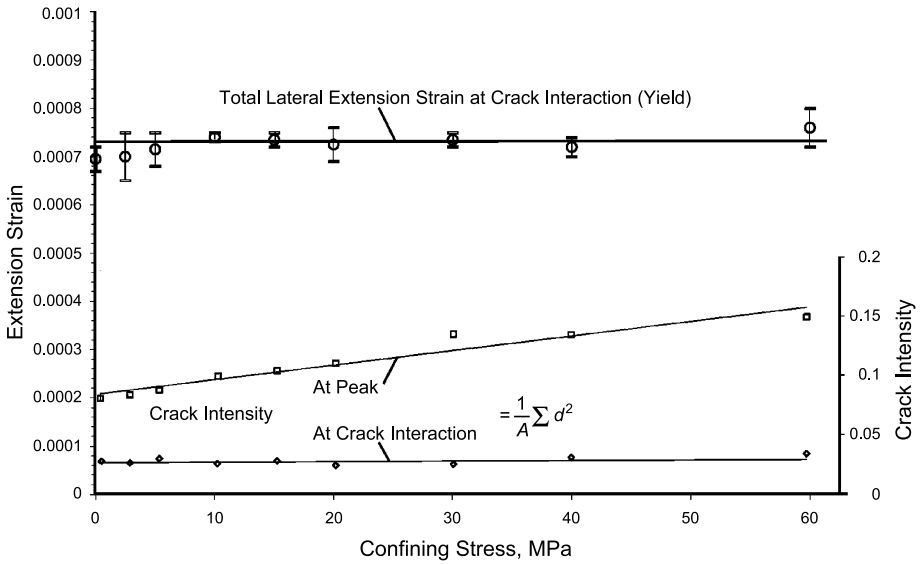
Fig. 31. Constant extension strain and crack intensity (A = sample area; d = grain size) at the point of critical crack interaction for confined compression tests. Crack intensity at peak deviatoric stress is shown for comparison
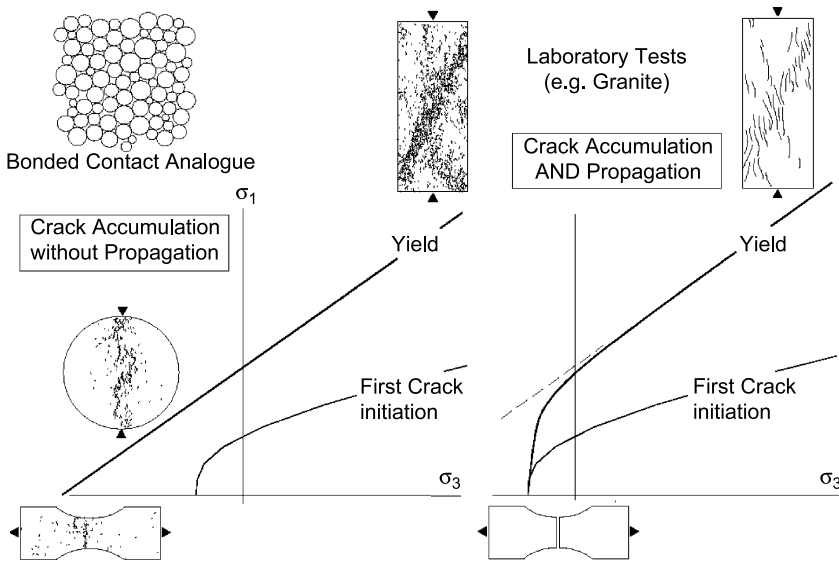
Fig. 32. Crack damage initiation and crack interaction (yield) thresholds for **a**) bonded contact simulations (no unstable crack propagation), **b**) actual rock samples (unstable crack propagation in tension)

therefore for upper bound rockmass strength, is not the result of conventional sliding friction, but rather of the elastic generation of extension strain and tensile crack accumulation in which friction plays no part.
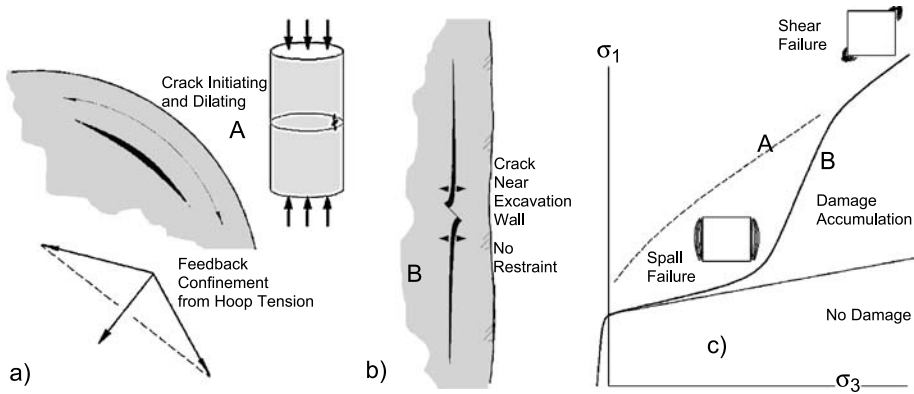
Fig. 33. a) Generation of feedback confinement during microcrack dilation; **b**) No such restraint in crack near excavation wall; **c**) Resultant drop in in situ strength due to crack propagation near boundary

Interestingly, this critical crack intensity, critical extension strain and the linearity crack interaction threshold in stress space are consistent for discrete element simulations (using simple bond model) of Brazilian tests, confined tension tests and uniaxial tension tests (Fig. 32a). In the absence of unstable isolated crack propagation, as is the case in the PFC models, crack accumulation and interaction must still take place as in confined compression. On the other hand, if crack propagation is permitted, a more realistic behaviour results as in Fig. 32b. In real rock, isolated cracks propagate under tensile conditions resulting in instantaneous failure after initiation in direct tension tests as shown.

The mechanics of crack propagation are the key to understanding the reduction in in situ strength below the true yield threshold for lab samples in Fig. 32b. In standard tests on cylindrical laboratory samples, initiating cracks within the sample must dilate in order to extend. This dilation creates a hoop tension in the rock radially beyond the crack which in turn creates increased confining stress arresting the crack as shown in Fig. 33a. Adjacent to an excavation, however, this feedback confinement is not present, and the initiating crack is free to propagate. In the extreme, in combination with other factors discussed in the next section, the in situ strength (observed failure strength) drops to the crack initiation threshold under near-boundary low confinement conditions favourable to fracture propagation and spalling as in Fig. 33b.

3.4 In Situ Strength Reduction

Other mechanisms compound to exacerbate crack propagation near excavation boundaries even if the apparent (average) stress field is fully compressive. These include scale effects related to the inclusion of weak links in a larger volume as well as scale effects related to the exchange of strain energy between a volume and a propagating surface. These effects also include unloading damage and oblique damage due to stress rotation, confinement loss due to open cracks, crack-surface interaction (and
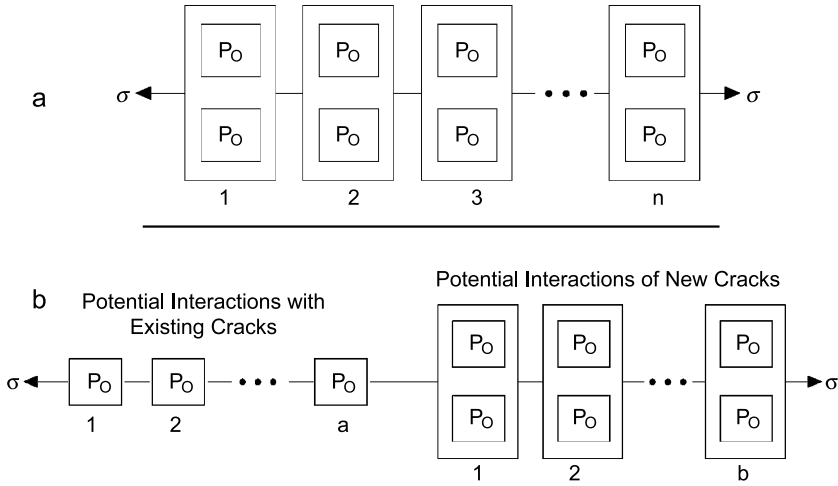
Fig. 34. **a**) Simple series-parallel reliability model based on Jardine (1973) – failure of system occurs when both units within an individual cell fail (two interacting cracks). **b**) a modified model representing potential interactions with pre-existing cracks

enhanced crack propagation), and heterogeneity and induced local tension. These factors combine adjacent to an excavation to reduce the upper bound yield strength towards the lower bound defined by initiation as shown in Figs. 18 and 33b.

To help explain the impact of some of these factors on interaction (yield) potential, a new statistical model for interaction was developed based on a series-parallel combination of interacting elements with Weibull strength distribution as illustrated in Fig. 34. The functions defining the probability of yield at a given stress and alternately the yield stress at a given probability are:

$$P_V(\sigma) = 1 - \left(1 - \left(1 - \exp\left[-\left(\frac{\sigma - \sigma_i}{\sigma_0}\right)^m\right]\right)^k\right)^{\frac{x}{2}\left(\frac{V}{V_0}\right)} \quad \text{for } \sigma > \sigma_i \quad (6)$$

$$\sigma = \sigma_0\left(-\ln\left(1 - \left(1 - (1 - P_V(\sigma))^{\left(\frac{x}{2}\frac{V}{V_0}\right)^{-1}}\right)^{\frac{1}{2}}\right)\right)^{\frac{1}{m}} + \sigma_i, \quad (7)$$

where $P_V(\sigma)$ is a specified yield probability; m, σ_i and σ_0 are Weibull probability parameters, V_0 is the grain volume (or area), V is the sample volume (or area), and x is the number of possible of interactions per crack (approximately 4 for PFC samples). In the series-parallel combination in Fig. 34a, the system fails (yield threshold) when two adjacent elements have yielded. The model is calibrated for crack initiation with real samples or in this case, with the discrete element model. Scale effects related to weak link inclusion are incorporated through increasing V while heterogeneity is defined by the parameter m.

Both the discrete element simulation and the statistical model can be used to demonstrate the effects of preexisting damage. The PFC model can incorporate distributions of pre-loading cracks in both isotropic and preferentially oriented fashion. Such cracks are a part of the unloading process and are discussed extensively by

Martin and Stimpson (1994). Pre-existing cracks do not necessarily contribute to a lower initiation threshold for new damage but rather create more possibilities for crack interaction as new damage develops. The total number of new cracks required for interaction, and therefore the total deviatoric stress level required for yield decreases. The revised model is schematically illustrated in Fig. 34b where $a = 4\chi V/V_0$ represents the number of possible interactions with pre-existing cracks and $b = (2 - 4\chi)V/V_0$ represents the number of potential "virgin" interactions. The probability of yield for damaged samples with a pre-existing crack intensity of χ, is given by:

$$P_V(\sigma) = 1 - \exp\left(-\left(\frac{\sigma - \sigma_i}{\sigma_0}\right)^m \cdot \frac{4\chi V}{V_0}\right)$$

$$\times \left(1 - \left(1 - \exp\left(-\left(\frac{\sigma - \sigma_i}{\sigma_0}\right)^m\right)\right)^k\right)^{\frac{(2-4\chi)V}{V_0}}. \qquad (8)$$

Figure 35 compares the yield predictions for samples with pre-existing isotropic damage based on a modified statistical model to PFC simulations of samples with both isotropic and preferentially oriented cracks prior to this loading stage.

Crack propagation length is incorporated by allowing the number of potential interactions, x, to become a function of the square of crack propagation length. The probability of yield at a given stress, σ, for a sample with pre-existing damage and the
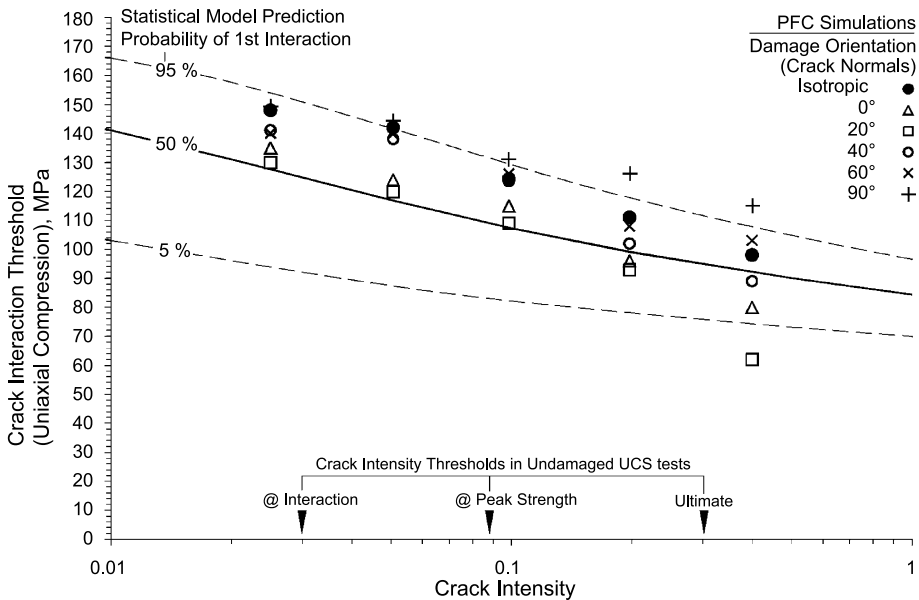
Fig. 35. Comparison of statistical yield model (including effects of pre-existing cracks as in Eq. (8) with results from PFC modelling. Model samples had varying degrees of pre-loading damage (isotropic and preferentially oriented as shown). Annotation above horizontal axis shows crack intensities at stages in a UCS test without pre-existing damage

freedom for crack propagation, after initiation, to a relative length of L^* (normalized to grain size) is given by:

$$P_V(\sigma) = 1 - \exp\left(-\left(\frac{\sigma - \sigma_i}{\sigma_0}\right)^m \cdot \frac{4f(L^*)\chi_0 V}{V_0}\right)$$

$$\times \left(1 - \left(1 - \exp\left(-\left(\frac{\sigma - \sigma_i}{\sigma_0}\right)^m\right)\right)\right)^{k}\Big\rangle^{\frac{V}{V_0}(2(L^*)^2 - 4f(L^*)\chi_0)}. \qquad (9)$$

In this model it is assumed that cracks grow to relative length L^* immediately upon initiation (stable crack propagation length is a function of increasing stress after initiation). It can also be assumed that pre-existing damage does or does not extend upon loading. In the first case pre-existing damage spontaneously extends to length L^* upon loading such that $f(L^*) = (L^*)^2$ in Eq. (9). In the second extreme, pre-existing cracks do not extend (but can still interact with extending new cracks) and have a constant length equal to the elemental dimension such that $f(L^*) = ((1 + L^*)/2)^2$ in Eq. (9). In Fig. 36 the composite result is shown for both assumptions regarding the propagation of pre-existing cracks. The model parameters are based on the $P = 50\%$ calibration (probability for systematic damage initiation).

The impact of enhanced propagation on yield strength is clearly demonstrated using the PFC simulations and the statistical model. While the PFC model does not adequately reflect unstable propagation of cracks, fracture mechanics can be employed to investigate the impact of confinement reduction near excavation boundaries on crack extension and spalling. Combining the critical Mode I stress intensity factor
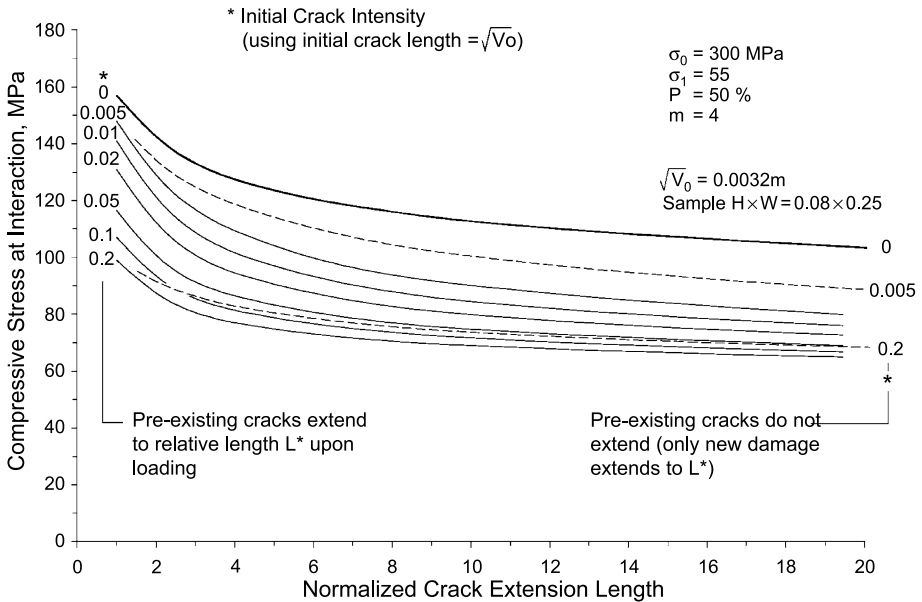
Fig. 36. Results of statistical yield model reflecting the effects of both crack extension and pre-existing damage (Eq. (9))

for an isolated sliding crack of length $2c$ and $\mu = \tan\phi$ and with propagating wing cracks each of length a is given by Ashby and Hallam (1986):

$$K_I = \frac{-\sigma_1\sqrt{\pi c}}{(1+L)^{\frac{3}{2}}}\{1 - \lambda - \mu(1+\lambda) - 4.3\lambda L\}\left\{0.23L + \frac{1}{\sqrt{3(1+L)}}\right\}, \qquad (10)$$

with a further relationship incorporating the effect of confinement and crack length on crack interaction with a free surface (Ashby and Hallam, 1986):

$$K_I^{surf} = \frac{1}{2\sqrt{2\pi}}\left(\frac{c}{t}\right)^{\frac{1}{2}}\sigma_1\sqrt{\pi c}\left[\frac{1 - \frac{4}{\sqrt{(3\sqrt{2})}}\frac{c}{t}\left(L + \frac{1}{\sqrt{2}}\right)^2\lambda}{1 + \frac{12}{\pi^2}\frac{c^2}{t^2}\left(L + \frac{1}{\sqrt{2}}\right)^2\frac{\sigma_1}{E}}\right], \qquad (11)$$

where $\lambda = \frac{\sigma_3}{\sigma_1}$ and $L = \frac{a}{c}$. The orientation, θ (angle of crack normal with respect to horizontal), of the critical flaw is incorporated into this derivation and is equal to $\frac{1}{2}\tan^{-1}\left(\frac{1}{\mu}\right)$. E is the Young's Modulus of the intact material. For simplicity, a 45 degree crack is used in the derivation of K_I^{surf}. Near a free boundary, a beam of thickness, t, is formed by the propagating crack. As the beam becomes more narrow (as the crack grows) it bends and allows further freedom of movement on the initial sliding flaw. This additional displacement, in turn, increases the stress intensity factor at the crack tip leading to further propagation. A similar result is obtained using an alternative formulation by Dyskin and Germanovich (1993). Combining the effects of the propagating flaw and the surface interaction and presuming that extension occurs when $(K_I + K_I^{surf})$ exceeds K_{IC} (critical intensity factor), the following relationship can be derived for critical (minimum) σ_3 required for stability.

Combining Eq. (10) and (11), setting $(K_I + K_I^{surf})$ to K_{IC}, and then solving for critical σ_3:

$$\sigma_3 = \frac{\sigma_1\left(C_1(1-\mu) + \frac{C_2}{1+C_4\sigma_1}\right) - \frac{K_{IC}}{\sqrt{\pi c}}}{C_1(1+\mu+4.3L) + \frac{C_2 C_3}{(1+C_4\sigma_1)}}, \qquad (12)$$

where:

$$C_1 = \left(0.23L + \frac{1}{\sqrt{3(1+L)}}\right)\frac{1}{(1+L)^{3/2}}, \qquad C_2 = \frac{1}{2\sqrt{2\pi}}\left(\frac{c}{t}\right)^{\frac{1}{2}},$$

$$C_3 = \frac{4\left(1+\frac{1}{\sqrt{2}}\right)^2}{\sqrt{(3\sqrt{2})}}\left(\frac{c}{t}\right) \quad \text{and} \quad C_4 = \frac{12}{\pi^2 E}\left(1+\frac{1}{\sqrt{2}}\right)^2\left(\frac{c}{t}\right)^2.$$

In the case of tensile stresses large enough to separate the surfaces of the initial (sliding) flaw, the critical σ_3 is given by:

$$\sigma_3 = \frac{-K_{IC}}{\sqrt{\pi c(L + \sin\theta)}}. \qquad (13)$$

Using the standard Kirsch solution for elastic stresses around a circular opening in an anisotropic stress field, and iteratively solving for the critical crack extension (L in
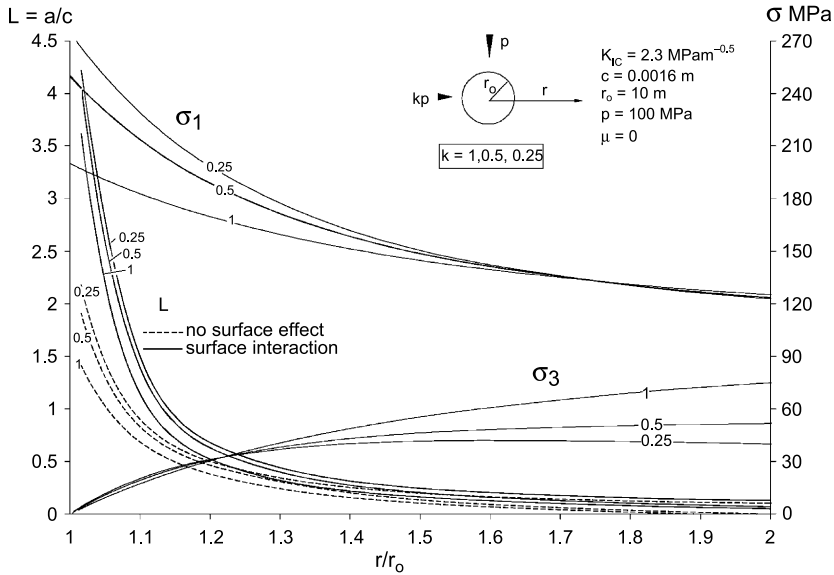
Fig. 37. Impact of near surface confinement and surface interaction on propagation of individual cracks after initiation as in Eqs. (10), (11) and (12). Stresses based on Kirsch solution

Eq. (10)) with and without the added impact of surface feedback (Eq. (11)), Fig. 37 can be generated to illustrate the effect of stress gradient and surface effects on the propagation of newly initiated cracks around a tunnel or borehole in hard rock (granite used for parametric purposes). If the impact of confinement on crack length as in Fig. 37 is considered along with the impact of crack propagation on the reduction of yield stress shown in Fig. 36, it is clear that the real near-excavation in situ strength must be considerably lower than the upper bound interaction threshold in laboratory testing.

Another strength reduction mechanism examined in Diederichs (2000) is the effect of internal heterogeneity and internal local tension. It is often argued that tensile failure cannot occur in a confined state. However, most rocks and rock masses are heterogeneous at the grain or rock block level and this introduces internal stress variations as illustrated by Fig. 28. When continuum models are adopted to determine the stability of an excavation, uniform stresses are predicted (implicit in homogeneous continuum models) with mostly confined conditions near excavations, unless irregular geometries or high in situ stress ratios cause tension zones. Figure 38 illustrates that this is not the case in heterogeneous rock masses. Here, the average stresses sampled within smaller regions of the overall confined specimen (20 MPa) are shown for applied axial stress levels of 80 and 250 MPa, respectively. The relative dominance of tensile zones (leading to the definition of a spalling limit defined by the slope σ_1/σ_3) will depend on the degree of heterogeneity within the rock, the level of in situ damage, the degree of stress rotation and disturbance during excavation.

Simulations at different confining stresses confirm that a constant confining stress ratio corresponds to equivalent spatial coverage of tensile zones (Fig. 39). The spatial
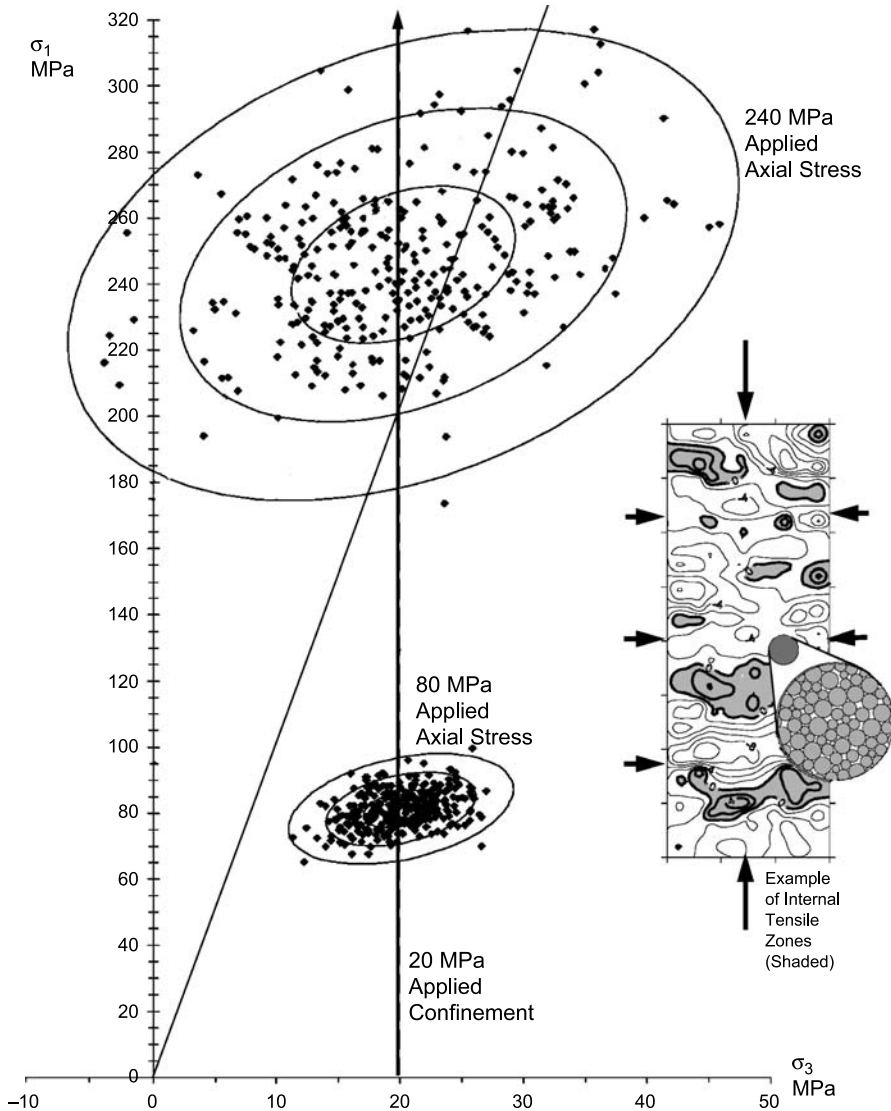
Fig. 38. Variation in local average stress (each dot represents the average stress within a sampling circle – Fig. 30a.) within a heterogeneous sample tested in compression under an applied confining stress of 20 MPa. Applied vertical stress states at 80 MPa and at 250 MPa are shown. Heterogeneity leads to internal tension which in turn leads to crack propagation and strength reduction in real solids

coverage required for spalling failure and the corresponding critical σ_3/σ_1 ratio is governed by heterogeneity, excavation damage and variability in surface geometry. This ratio, in practice, is normally between 10 and 20. The spalling limit is then combined with the damage initiation (lower bound) threshold and the crack interaction threshold (upper bound) to give the composite stress path limit in Fig. 18.
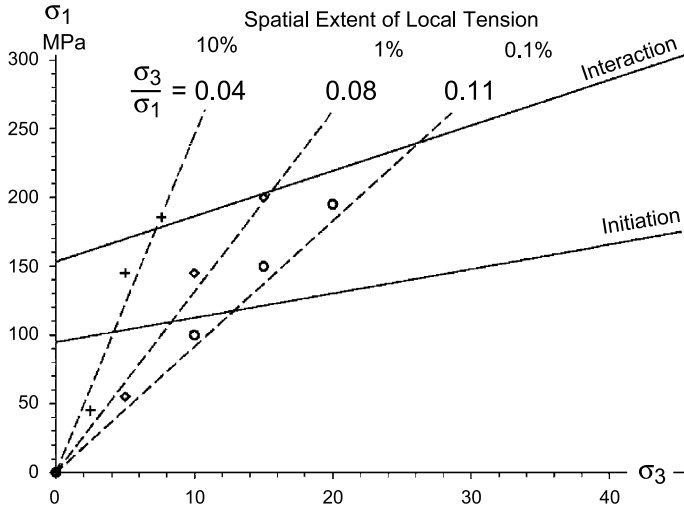
Fig. 39. Spalling limits (after Diederichs, 2002) defined as zones of equal spatial coverage for tensile zones (from discrete element simulations)

The combination of the factors summarized here leads, in the extreme, to a complete collapse of the in situ yield limit from an upper bound. The end result is the multiphase in situ strength envelope introduced in Fig. 17, incorporating the effects of tensile damage initiation and accumulation with strength reduction due to uncontrolled propagation in near-excavation conditions.

4. Conclusions

A brief summary of key findings of Diederichs (2000) is presented here, separated into two sections relating to the influence of tensile damage processes an confinement loss or relaxation.

4.1 Structurally Controlled Instability

The significant impact of remnant rock bridges is demonstrated in this thesis. As shown using a fracture mechanics approach, even a relatively small percentage of intact area in the plane of a joint (e.g. less than 1%) can provide a distributed load capacity equal to heavy support systems used in hard rock mining today. This impact is quantified using wedge stability calculations and using the modified voussoir beam approach.

This internal or natural gravity support may be sensitive to long term weakening effects (stress corrosion, dynamic disturbance) but can be relied upon to provide adequate short-term support for efficient excavation cycling, development and stope extraction.

While civil excavations (tunnels, caverns) are designed to maintain compressive stress flow parallel to the surfaces of the openings (thereby increasing structural

stability), mining openings are constructed in accordance with operational requirements and ore geometries. As such, confinement loss and complete relaxation are common around geometrically complex mining excavations. The associated impact on stability is demonstrated and quantified.

Small amounts of confinement are required to mobilize frictional resistance on joint surfaces such that wedges or blocks become stable under gravity loading. Loss of this confinement is responsible for delayed failure of structurally defined rockmasses. Loss of confinement in laminated ground leads to increased gravity induced displacements and failure as demonstrated by an updated voussoir beam analogue.

A calibrated voussoir model is used to compute the impact of relaxation on empirical stability limits which do not explicitly consider this effect. Comparison to field data in which relaxation is identified as a major influence, show that the adjusted stability limit, determined with consideration of relaxation, accurately quantifies and predicts relaxation-induced instability in mining openings.

4.2 Stress Driven Instability

Both spalling and macroscopic shear rupture are shown to be the result of tensile damage initiation and accumulation. Microscopic shear initiation mechanisms only become dominant at very high confinements or at ultra-slow loading rates. At low to moderate, shear zone formation is the result of extension crack interaction.

Macroscopic or inter-granular friction is not a factor in the damage process until well after the peak strength has been exceeded and fully localized failure has developed.

Crack initiation (crack nucleation at the weakest elements) is dependent on deviatoric stress and is relatively insensitive to confinement. Crack accumulation is a stochastic process in a heterogeneous solid. Yield is related to a critical probability of crack interaction which in turn is associated with a critical amount of accumulated lateral extension strain (normal to major compression). Crack interaction marks the onset of true yield, and determines the upper bound for long-term, sample and geometry independent strength in laboratory tests. If crack extension length is increased, crack interaction and yield occur with less crack accumulation (fewer individual crack nucleations) and therefore at a lower compressive stress level.

A number of mechanisms, all investigated in this thesis, reduce the crack interaction threshold near excavations in situ. These include scale effects, pre-existing and excavation induced damage, crack – surface interaction and enhanced crack propagation, and heterogeneity-induced local tension.

The stress threshold for crack initiation is unaffected by these factors. The cumulative impact of these mechanisms, however, is to reduce the in situ yield strength, near excavation boundaries, to a lower bound defined by the threshold for crack initiation. The important implications for tunnel design and support optimization, of this lower bound strength and of the characteristics of spalling failure, are developed and discussed in more detail in Kaiser et al. (2000).

Elastic stress path analysis can be compared to a multiphase threshold (Fig. 18) to predict relaxation induced blockfall, boundary parallel spalling or confined shear accompanied or preceded by micro-seismicity.

Acknowledgements

References

Ashby, M. F., Hallam, S. D. (1986): The failure of brittle solids containing small cracks under compressive stress states. Acta Metall. 34(3), 497–510.

Atkinson, B. K., Meredith, P. G. (1987): The theory of subcritical crack growth with applications to minerals and rocks. Fracture mechanics of rock. Academic Press, London, 111–167.

Barton, N. R., Lien, R., Lunde, J. (1974): Engineering classification of rock masses for the design of tunnel support. Rock Mech. 6(4), 189–239.

Bawden, W. F. (1993): The use of rock mechanics principles in Canadian hard rock mine design. Comprehensive rock engineering 5. Pergamon Press, Oxford, 247–290.

Beer, G., Meek, J. L. (1982): Design curves for roofs and hangingwalls in bedded rock based on voussoir beam and plate solutions. Trans. Inst. Min. Metall. 91, A18–A22.

Brace, W. F., Paulding, B. W., Scholz, C. (1966): Dilatancy in the fracture of crystalline rocks. J. Geophys. Res. 71(16), 3939–3953.

Brady, B. H. G., Brown, E. T. (1993): Rock mechanics for underground mining. Chapman and Hall, London, 571p.

Brown, E. T., Trollope, D. H. (1967): The failure of linear brittle materials under effective tensile stress. Rock Mech. Engng. Geol. 5, 229–241.

Castro, L., McCreath, D., Kaiser, P. K. (1995): Rockmass strength determination from breakouts in tunnels and boreholes. Proc., 8th ISRM Congress, Tokyo, 2, 531–536.

Castro, L., McCreath, D., Oliver, P. (1996): Rockmass damage initiation around the Sudbury Neutrino Observatory Cavern. In: Aubertin, et al. (eds.) Rock mechanics-NARMS '96, 2, Balkema, Rotterdam, 1589–1595.

Cook, N. G. W. (1995): Müller Lecture: Why rock mechanics? 3, Proc. Int. Cong. on Rock Mechanics. Tokyo, 975–994.

Diederichs, M. S. (2000): Instability of hard rockmasses: The role of tensile damage and relaxation. PhD Thesis, University of Waterloo, 566p.

Diederichs, M. S. (2002): Keynote: Stress induced accumulation and implications for hard rock engineering. In: Hammah, R., Bawden, W., Curran, J., Telesnicki, M. (eds.) Proc., NARMS 2002, Toronto, University of Toronto Press, 3–14.

Diederichs, M. S., Kaiser, P. K. (1999a): Tensile strength and abutment relaxation as failure control mechanisms in underground excations. Int. J. Rock Mech. Min. Sci. Geomech. Abstr. 36, 69–96.

Diederichs, M. S., Kaiser, P. K. (1999b): Stability of large excavations in laminated hard rock masses: the voussoir analogue revisited. Int. J. Rock Mech. Min. Sci. Geomech. Abstr. 36, 97–117.

Dyskin, A. V., Germanovich, L. N. (1993): Model of rockburst caused by cracks growing near free surface. Rockbursts and seismicity in mines. Balkema, Rotterdam, 169–174.

Eberhardt, E., Stead, D., Stimpson, B., Read, R. S. (1998): Identifying crack initiation and propagation thresholds in brittle rock. Cana. Geotechn. J. 35(2), 222–233.

Evans, W. H. (1941): The strength of undermined strata. Trans. Inst. Min. Metall. 50, 475–500.

Fonseka, G. M., Murrell, S. A. F., Barnes, P. (1985): Scanning electron microscope and acoustic emission studies of crack development in rocks. Int. J. Rock Mech. Min. Sci. Geomech. Abstr. 22(5), 273–289.

Fowell, R. J., Xu, C. (1994): The use of the cracked Brazilian disc geometry for rock fracture investigations. Int. J. Rock Mech. Min. Sci. Geomech. Abstr. 31(6), 571–580.

Greer, G. J. (1989): Empirical modelling of open stope stability in a vertical crater retreat application at INCO's Thompson Mine. 91st Canadian Institute of Mining AGM, 12p.

Hoek, E. (1968): Brittle failure of rock. In: Stagg, K. G., Zienkiewicz, O. C. (eds.) Rock mechanics in engineering practice, 99–124.

Hommand, F., Hoxha, D., Shao, J. F., Sibai, M., Duveau, G. (1995): Endommagement de granites et de marnes: Essais mechaniques, identification des parameters d'un modele d'endommagement et simulation. Final Report B RP O.ENG/O.LML 95.015. ENGS Laboratoire de Géomécanique, Nancy.

Hutchinson, D. J. (1998): Intersection Support Demand Assessment Guidelines. Report to INCO Mines Technical Services.

Hutchinson, D. J., Diederichs, M. S. (1996): Cablebolting in underground mines. Bitech Publishers, Vancouver, 416p.

Illston, J. M., Dinwoodie, J. M., Smith, A. A. (1979): Concrete, timber and metals. Van Nostrand Reinhold, New York, 663p.

Ingraffea, A. P. (1987): Theory of crack initiation and propagation in rock. In: Fracture mechanics of rock. Academic Press, London, 71–110.

Irwin, G. R. (1957): Analysis of stresses and strains near the ends of a crack traversing a plate. J. Appl. Mech. 24, 361–364.

Itasca (1995): PFC-particle flow code. Modelling Software. Version 1.0. Itasca Ltd.

Jardine, A. K. S. (1973): Maintenance, replacement and reliability. Pitman, London, 200p.

Kaiser, P. K., Diederichs, M. S., Martin, D., Sharp, J., Steiner, W. (2000): Invited keynote: underground works in hard rock tunnelling and mining. GeoEng2000, Melbourne. Pennsylvania: Technomic Publishing, 841–937.

Kaiser, P. K., Yazici, S., Nosé, J. (1992): Effect of stress change on the bond strength of fully grouted cables. Int. J. Rock Mech. Min. Sci. Geomech. Abstr. 29(3), 293–306.

Kaiser, P. K., Yazici, S., Maloney, S. (2001): Mining induced stress change and consequences of stress path on excavation stability – a case study. Int J. of Rock Mech. Min. Sci. 38(2), 167–180.

Kemeny, J. M., Cook, N. G. W. (1986): Effective moduli, non-linear deformation and strength of a cracked elastic solid. Int. J. Rock Mech. Min. Sci. Geomech. Abstr. 23(2), 107–118.

Landriault, D., Oliver, P. (1992): The destress slot concept for bulk mining at depth. In: Kaiser, P. K., McCreath, D. R. (eds.) Rock Support in mining and underground construction. Balkema, Rotterdam, 211–217.

Laqueche, H., Rousseau, A., Valentin, G. (1986): Crack propagation under Mode I and II loading in slate schist. Int. J. Rock Mech. Min. Sci. Geomech. Abstr. 23(5), 347–354.

Maloney, S. M., Kaiser, P. K. (1991): Stress change and deformation monitoring for mine design: A case study. Field measurements in geomechanics. Balkema, Rotterdam, 481–490.

Martin, C. D. (1994): The Strength of massive Lac du Bonnet granite around underground openings. Ph.D. Thesis. University of Manitoba.

Martin, C. D. (1997): Seventeenth Canadian Geotechnical Colloquium: The effect of cohesion loss and stress path on brittle rock strength. Can. Geotech. J. 34(5), 698–725.

Martin, C. D., Kaiser, P. K., McCreath, D. R. (1999): Hoek-Brown parameters for predicting the depth of brittle failure around tunnels. Can. Geotech. J. 36(1), 136–151.

Martin, C. D., Stimpson, B. (1994): The effect of sample disturbance on laboratory properties of Lac du Bonnet granite. Can. Geotech. J. 31, 692–702.

Nickson, S. D. (1992): Cable support guidelines for underground hard rock mine operations. M.A.Sc. Thesis, Dept. of Mining and Mineral Processing, University of British Columbia, 343p.

Obert, L., Duvall, W. I. (1966): Rock mechanics and the design of structures in rock. John Wiley and Sons, Chichester, 649p.

Okubo, S., Fukui, K. (1996): Complete stress-strain curves for various rock types in uniaxial tension. Int. J. Rock Mech. Min. Sci. Geomech. Abstr. 33(6), 549–556.

Pelli, F., Kaiser, P. K., Morgenstern, N. R. (1991): An interpretation of ground movements recorded during construction of the Donkin-Morien tunnel. Can. Geotech. J. 28(2), 239–254.

Pestman, B. J., Van Munster, J. G. (1996): An acoustic emission study of damage development and stress-memory effects in sandstone. Int. J. Rock Mech. Min. Sci. 33(6), 585–593.

Potvin, Y. (1988): Empirical open stope design in Canada. Ph.D. Thesis, Dept. of Mining and Mineral Processing, University of British Columbia, 343p.

Potvin, Y., Milne, D. (1992): Empirical cablebolt support design. In: Kaiser, P. K., McCreath, D. R. (eds.) Rock support, A. A. Balkema, Rotterdam, 269–275.

Sih, G. C. (1973): Handbook of stress intensity factors. Inst. of Fracture and Solid Mechanics, Lehigh University, Bethlehem.

Stacey, T. R. (1981): A simple extension strain criterion for fracture of brittle rock. Int. J. Fract. 18, 469–474.

Stillborg, B. (1994): Professional users handbook for rock bolting. TransTech, Germany, 164p.

Tapponier, P., Brace, W. F. (1976): Development of stress induced microcracks in Westerly granite. Int. J. Rock Mech. Min. Sci. Geomech. Abstr. 13, 103–112.

Weibull, W. (1951): A statistical distribution function of wide applicability. J. Appl. Mech., September, 293–297.

Wiles, T. D. (1996): MAP-3D Version 36. A mining analysis program in three dimensions. Mine Modelling Ltd. Copper Cliff, Ontario.

Appendix I: Tensile Fracture Strength Models

Stress intensity relationships for internal and external cracks in plates (Irwin, 1957; Sih, 1973; Kemeny and Cook, 1986) can be extended for isolated cracks and rock bridges in three dimensions. For a given Mode I stress intensity factor at crack extension K_{IC}, the tensile strength for a partially cracked solid can be computed for circular non-interacting cracks of radius c, with crack normals oriented at angle γ to the direction of tensile loading:

$$\sigma_T = K_{IC} \left(\frac{\pi}{2\sqrt{\pi c}} \right) \frac{1}{\cos^2 \gamma}. \tag{I.1}$$

Using Kemeny and Cook's (1986) external crack solution, the tensile strength of a cylinder of rock with a total cross sectional area, A, containing a circular rock bridge of radius a (surrounded by a planar, annular crack) is given by:

$$\sigma_T = K_{IC}\left(\frac{2a\sqrt{\pi a}}{A}\right)\frac{1}{\cos^2\gamma}. \tag{I.2}$$

If N/V is the number of regularly distributed cracks or rock bridges in a unit cubic volume $(V = 1\,\text{m}^3)$, then the total coplanar cross sectional area (cracked and uncracked) associated with the crack or rock bridge, A is:

$$A = \frac{1}{N^{2/3}}. \tag{I.3}$$

If $(A_c{}^*)A$ is the area of the crack and $(A_a{}^*)A$ is the area of the rock bridge ($A_c{}^*$ and $A_a{}^*$ are the ratios of cracked and intact area, respectively, to the total cross section):

$$c \approx \sqrt{\frac{A_c{}^*}{\pi N^{2/3}}}, \tag{I.4}$$

$$a \approx \sqrt{\frac{A_a{}^*}{\pi N^{2/3}}}, \tag{I.5}$$

where $A_a{}^* = 1 - A_c{}^*$.

The tensile strength with respect to the percentage of cracked cross sectional area for cracks perpendicular to loading ($\cos^2\gamma = 1$) is:

$$\sigma_T = \frac{\pi}{2}K_{IC}\sqrt{\frac{N^{1/3}}{\sqrt{\pi(A_c{}^*)}}} \quad \text{for } A_c{}^* \ll 1, \tag{I.6}$$

or inversely, with respect to percentage of intact rock bridges:

$$\sigma_T = 2K_{IC}\sqrt{\frac{(A_a{}^*)^{3/2}N^{1/3}}{\sqrt{\pi}}} \quad \text{for } A_a{}^* \ll 1. \tag{I.7}$$

For comparison with measurements of relative linear joint trace persistence, P, a regular array of circular cracks yields the approximate relationship for average linear persistence, P:

$$P = \psi\frac{c}{c+a} = \psi\frac{A_C{}^*}{1 + 2\sqrt{A_C{}^*(1 - A_C{}^*)}}, \tag{I.8}$$

where ψ is a factor which ranges from $1/\sqrt{2}$ to 1 for small (isolated) cracks and from 1 to $\sqrt{2}$ for rock bridges (extensive cracking), depending on the linear persistence measurement direction in the plane of the circular crack or rock bridge.

Appendix II: Voussoir Beam Model

The voussoir beam analogue of Brady and Brown (1993) was reviewed, updated and verified in Diederichs and Kaiser (1999b). The effects of relaxation were incorporated in Diederichs and Kaiser (1999a). The voussoir beam forms in laminated or blocky

ground when the resistance to tensile stress parallel to the laminations is reduced to zero by through-going fractures perpendicular to the beam. The symmetrical distribution of compression and tension through a cross-section of the elastic beam of thickness, T, is replaced by a compressive arch which varies in thickness but is typically between 0.5 and 0.75 times the beam thickness for a highly stable beam. Failure of slender beams is by snap-through or by crushing at the upper side of the beam at midspan where the compressive stress is the highest. Thicker beams can also fail through slip along the lamination normal joint set. The moment generated at the abutment by the self weight of the half-span must be balanced with the opposing moment generated by the offset reaction force, F, at the midspan. Two key independent unknowns are the thickness of the compressive arch, NT, and the moment arm between the reaction resultants at the abutment and at midspan, Z. The problem is statically indeterminate but can be solved in an iterative fashion.

The reaction distributions at the midspan and at the abutments are assumed to be identical such that the initial (Z_0) and final (Z) moment arms are given by:

$$Z_0 = T\left(1 - \frac{2}{3}N\right); \qquad Z = \sqrt{\frac{3S}{8}\left(\frac{8}{3S}Z_0^2 - \Delta L\right)}. \tag{II.1}$$

The deflection, D, at midspan is given by ($Z - Z_0$) and a negative value for the term under the square root sign in Eq. (4.2) indicates that the critical beam deflection for the assumed thickness, NT, has been exceeded. For a square span, elastic shortening of the effective internal arch ΔL, due to compression is calculated as:

$$\Delta L = \frac{\gamma S^2}{6EN(Z_0 + Z)}\left(\frac{2}{9} + \frac{N}{3}\right)\left(S + \frac{8}{3S}Z_0^2\right)(1 - v). \tag{II.2}$$

An iterative solution as described in Chapter 3 is used to find the parametric pair $(N, Z(N))$ which minimizes f_{max}, giving the equilibrium solution for the stable beam. The limit of stability is determined when no solution is possible in-range value of N and the beam fails by "snap-through". For the two dimensional case this point corresponds to a deflection at the midspan equivalent to approximately 25% of the thickness. A more conservative stability threshold is introduced based on the onset of snap-through instability (deviation from a linear deflection-thickness relationship). This limit corresponds to a deflection of 10% of the thickness and is defined by the parametric set which yields a minimum of 35% invalid values of N in the range 0 to 1. Maximum compressive stress can also be calculated and compared with limiting values for crushing failure.

Prior to calculating the shortening of the arch due to deflection and compression, it is possible to introduce an symmetrical displacement δ_A, acting in opposite directions at each abutment. This displacement yields a reduced initial moment arm, Z_0^*:

$$Z_0^* = \sqrt{\frac{3S}{8}\left(\frac{8}{3S}Z_0^2 - 2\delta_A\right)} \tag{II.3}$$

for substitution into Eq. (II.1).

For support pressure p or for surcharge loading, s such that $p = -s$ distributed evenly over the length of the beam, a solution can be obtained by substituting an equivalent unit weight, γ^*:

$$\gamma^* = \gamma - \frac{p}{T} \tag{II.4}$$

into Eq. (II.2).

Author's address: Ass. Prof. Mark Stephen Diederichs, Ph.D., Department of Geological Sciences and Geological Engineering, Queen's University, Kingston, ON K7L 3N6, Canada; e-mail: mdiederi@geol.queensu.ca